Applied Ocean Research 173 (2026) 105146

Contents lists available at ScienceDirect

Applied Ocean Research

journal homepage: www.elsevier.com/locate/apor

Research paper

Experimental study of wave-driven sediment suspension in flexible vegetation canopies with rippled beds

K. Ions [a,*], X. Wang [a], N. Mori [b], D.E. Reeve [a], H. Karunarathna [a]

[a] Centre for Nature-based Solutions, Faculty of Science and Engineering, Swansea University, Bay Campus, Fabian Way, Swansea SA1 8EN, UK
[b] Disaster Prevention Research Institute, Uji Campus, Kyoto University, Gokasho, Uji, Kyoto 611-0011, Japan

ARTICLE INFO

Keywords:
Sediment suspension
Waves
Flexible vegetation
Nature based solution
Experimental study
Bedforms

ABSTRACT

Laboratory experiments have been used to investigate the impact of flexible vegetation on sediment suspension over rippled sandy beds. Flexible vegetation mimics were examined across a range of wave conditions and stem densities, with rigid vegetation cases included for comparison. Measurements of velocity and suspended sediment concentration were used to compare near-bed hydrodynamics, bedform response, and sediment resuspension within the vegetation canopies. The results show that stem flexibility does not modify the dominant mechanisms governing near-bed sediment suspension when ripples are present. Flexible vegetation did not significantly modify ripple crest height or wavelength relative to bare sediment beds ($p > 0.05$), whereas rigid vegetation disrupted ripple geometry in the majority of cases tested ($p < 0.05$). Flexible canopies produced modest, statistically non-significant reductions in near-bed velocity of 0–5% relative to bare-bed conditions, confined to the lower 25% of the stem height, compared to reductions of 14–23% under rigid canopies ($p < 0.001$), which was observed over the entire stem length. Near-bed TKE within flexible canopies was statistically indistinguishable from bare-bed values across all conditions tested ($p > 0.74$), consistent with suppression of stem-generated vortex shedding due to stem reconfiguration and the preservation of ripple-induced turbulence as the dominant near-bed TKE source. Near-bed suspended sediment concentration collapsed onto a single power-law relationship with near-bed velocity across all vegetation types, densities, and wave conditions ($R^2 = 0.97$), with good agreement obtained using bare-bed ripple formulations applied with measured near-bed velocities. The results indicate that, for wave propagation over vegetated rippled beds, sediment resuspension is governed primarily by bedform-scale processes rather than by vegetation-induced TKE. The findings contrast with flat-bed and dense-canopy studies and highlight the importance of explicitly accounting for bedforms when modelling sediment transport in vegetated coastal environments.

1. Introduction

Coastal wetlands occur in intertidal zones of sheltered, low-energy environments (Bouma et al., 2005; McOwen et al., 2017; Giri et al., 2011). These ecosystems provide numerous ecological benefits, including habitat provision, shoreline stabilisation, nutrient cycling, and water quality improvement (Temmerman et al., 2013; Himes-Cornell et al., 2018). Wetland vegetation plays a pivotal role in modifying hydrodynamics and promoting sediment retention, thus contributing to long-term elevation gain and resilience to sea-level rise (McKee et al., 2007; 2011; Furukawa et al., 1997).

Previous research has established that coastal vegetation attenuates wave energy and flow velocities (Yang, 1998; Koch and Gust, 1999; Gambi et al., 1990; Møller et al., 2014; Weitzman et al., 2015), reduces coastal erosion, and promotes sediment deposition (Horppila and Nurminen, 2003; Zhu et al., 2015; Reidenbach and Timmerman, 2019). These mechanisms drive the application of vegetated systems as nature-based solutions (NbS) for sustainable coastal management (Fagherazzi et al., 2017; Moritsch et al., 2022).Vegetation type and morphology significantly impact these processes. Coastal vegetation is often broadly categorised as either rigid or flexible, depending on flexural rigidity (*EI*), which typically spans several orders of magnitude from $\sim 10^{-6}$–10^{-3} N·m^2 (Mullarney and Henderson, 2010; Luhar and Nepf, 2011; Nepf, 2012). Rigid vegetation, such as mangroves (e.g., *Rhizophora mangle*) and woody salt marsh species (e.g., *Spartina patens, Juncus roemerianus*), can remain upright under wave forcing. In contrast,

* Corresponding author.
E-mail address: k.d.ions@swansea.ac.uk (K. Ions).

https://doi.org/10.1016/j.apor.2026.105146
Received 10 February 2026; Received in revised form 10 June 2026; Accepted 11 June 2026
Available online 16 June 2026

flexible vegetation, such as seagrass (e.g., *Zostera marina, Thalassia testudinum*) and some salt marsh species (e.g., *Spartina alterniflora*), bends or sways with the flow.

These differences in plant types lead to distinct stem-dynamics and flow dynamics. Rigid vegetation is associated with greater velocity attenuation and potentially higher TKE generation around vegetation, which can contribute to sediment suspension until vegetation coverage is sufficient to dampen flow velocity (Ros et al., 2014; Tinoco and Coco, 2018; van Veelen et al., 2025). Flexible vegetation, in contrast, generally produces lower levels of TKE, especially near the bed, and can support depositional conditions when canopy coverage is sufficient (Zhang et al., 2018; Ros et al., 2014; Grady, 1981; De Falco et al., 2000).Stem generated TKE is a known driver of sediment suspension, but another key contributor is the presence of wave-generated bedforms. Ripples, commonly observed on sandy seabed, induce vortex shedding that enhances near-bed TKE, and sediment resuspension (Nielsen, 1992; Williams and Kemp, 1971). The near-bed region, typically the lower portion of the water column within ~5 cm of the sediment surface (Thorne et al., 2002), is where these interactions are most pronounced.

Coastal vegetation naturally occurs on sandy seabeds, and ripple formation is common (Fig. 1; Mullaney et al., 2017). Most seagrasses are rooted in shallow sandy to muddy coastal sediments (den Hartog, 1970; Hemminga and Duarte, 2000), with sandy-substrate species spanning all four seagrass families (Widdows et al., 2008; Masselink et al., 2024; Gintowt et al., 2025). Sandy-substrate coastal vegetation extends beyond seagrasses, with saltmarsh pioneer species including *Spartina alterniflora, Salicornia, and Suaeda maritima* colonising both sandy and muddy sediments (O'Connor et al., 2011), and globally 21% of mangroves occupy open-coast settings characterised by sandier sediments, such as *Sonneratia alba, Avicennia marina* and *Rhizophora mucronata* (Worthington et al., 2020). Vegetation can interfere with or modify ripple-induced TKE, creating complex interactions between stem-generated and bedform-generated TKE (Ions et al., 2025). While vegetation is also frequently found in muddy and cohesive environments, these systems are not considered here to isolate vegetation–hydrodynamic interactions over sandy, mobile beds.

Previous studies investigated ripple development within rigid vegetation mimics (Ions et al., 2025) or flexible blades attached to rigid sheaths (Zhang and Nepf, 2019), which may act as rigid vegetation near the bed. These studies observed that, beyond a certain wave orbital excursion (A_w) relative to stem spacing(S_x) A_w/S_xor alternatively, wake factor ($WF = 2A_w 2b_v Nv$, where b_v and N_v are stem diameter and number of stems per meter^2), the stem generated TKE could flatten the bed and suppress ripple formation. However, these studies did not consider cases where vegetation is fully flexible, along its entire length, including in the near-bed region. These studies also did not establish whether vegetation-induced TKE remains the primary control on sediment suspension once wave-generated bedforms are present. Given the observed effects of plant flexibility on flow structure and TKE production (Tinoco and Coco, 2018; Zhang et al., 2018; Ros et al., 2014), the influence on bedform development and resultant sediment transport needs further investigation.

This study focuses on fully flexible vegetation and its influence on sediment suspension and bedform development under wave forcing. Our previous work (Ions et al., 2025), which examined rigid vegetation dynamics, will be used as a benchmark to isolate the role of flexible vegetation in shaping coastal sediment processes. The stem-wave interactions, TKE, near-bed sediment suspension, and ripple formation are compared to those with rigid vegetation to assess the role of vegetation flexibility on ripple formation and sediment suspension. The findings contribute to our understanding of the complex feedback between the morphodynamics and vegetated coastal system. Section 2 outlines the theoretical background relevant to ripple formation and sediment transport in vegetated seabeds. Section 3 describes the experimental methodology, including data scaling procedures and post-processing techniques. Results and discussions are presented in Section 4 and Section 5, with a focus on velocity attenuation, TKE generation, near-bed sediment concentration, and ripple characteristics. Finally, conclusions are drawn in Section 5.

2. Theoretical background of sediment dynamics and ripple formation

Sediment transport on a sandy seabed occurs when the near-bed shear stress acting on sediment exceeds the critical threshold for sediment movement. There are two predominant processes of sediment movement: i) bedload/saltation, where sediment is transported by rolling, sliding, or bouncing along the seabed, and ii) suspended sediment, where sediment is suspended in the water column above the bed layer. This paper focuses on suspended sediment transport, specifically, the near-bed reference suspended sediment concentration, C_0. C_0 was selected since it is the boundary condition used in the vertical sediment flux models over rippled beds (e.g., Thorne et al., 2009) and the quantity which is most directly governed by near-bed processes.

Sediment motion is initiated when wave-induced near-bed velocities exceed a critical threshold, which depends on sediment properties and bed roughness (van Rijn, 1984; Soulsby, 1997). This threshold can be calculated by determining the threshold velocity for motion, U_{thresh}, which can be defined by Eq. (1), following Komar and Miller (1973).

$$\frac{\rho U_{thresh}^2}{(\rho_s - \rho) g D_{50}} = 0.30 \left(\frac{2A_w}{D_{50}} \right)^{0.5} \quad (1)$$

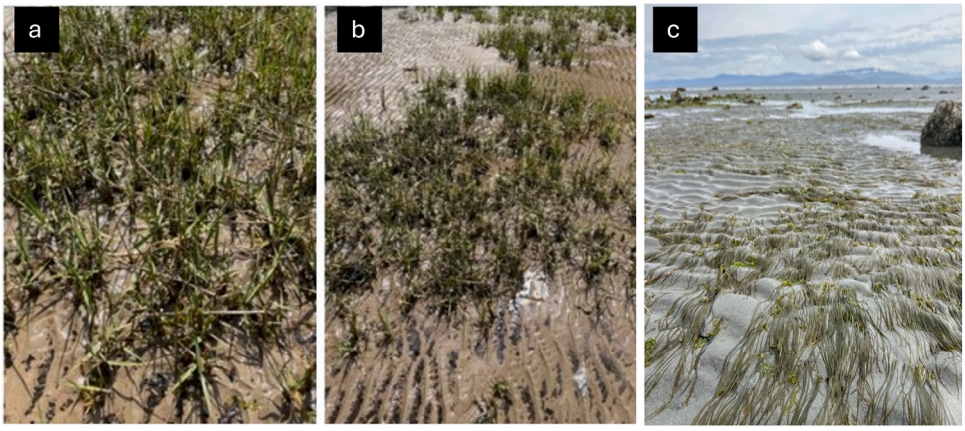

Fig. 1. Field photographs showing ripple formation within seagrass canopies during low tide at Llyn Peninsula, North Wales. Panels (a)–(c) illustrate the prevalence of bedforms within vegetated coastal environments, highlighting the interaction between vegetation and sediment morphology.

for rippled beds, A_w is the horizontal water particle excursion, $A_w = U_{bed}T/2\Pi$ and T is the wave period, ρ_s and ρ are the densities of the sediment and water, respectively, g is the acceleration due to gravity and D_{50} is the median sediment diameter.

Multiple criteria exist to describe the critical velocity, which results in critical bed shear stress for the sediment movement (van Rijn, 1984; Soulsby, 1997; Komar and Miller, 1973). Sediment movement over a flatbed is often determined by the shield parameter θ' expressed as.

$$\theta' = \frac{\tau_b}{(\rho_s - \rho)gD_{50}} \tag{2}$$

where $\tau_b = 0.5pf_wU_{bed}^2$ is the bed shear stress induced by waves on sediment. The wave friction factor (skin friction) f_w, which was derived by Swart (1974), can be expressed as.

$$f_w = \exp\left[5.213\left(\frac{k_b}{A_w}\right)^{0.194} - 5.977\right] \tag{3}$$

k_b is the roughness, given as $2.5D_{50}$ for flat beds and $k_b = \delta_r\eta_r^2/\lambda_r$, for rippled beds, and T is the wave period.

Under wave action, there are three main types of ripples formed on sandy seabeds: (i) orbital ripples, which form under smaller values of A_w/D_{50}, typically < 2000, here the ripple wavelength, $\lambda_r$is proportional to D_{50}; (ii) anorbital ripples which form for reasonably large values of A_w/D_{50} typically > 5000 and λ_r is approximately equal to $500 \times D_{50}$ and (iii) sub-orbital ripples, which form in the transitional region between orbital and anorbital ripples (Clifton, 1976). Orbital ripples were observed in this study for the sediment type under the range of conditions tested. Following the methodology of Thorne et al. (2002), if ripple steepness $\eta_r/\lambda_r > 0.12$ where η_r is the ripple crest height, ripples are considered steep enough to form vortices and suspend sediment. If no ripple is present or $\eta_r/\lambda_r < 0.12$, then those cases are considered flat-sandy-bed cases. Previous studies on sediment suspension over vegetated sandy beds have shown a reduced velocity threshold compared to bare sediment beds, which decreases with increasing stem solid volume fraction ($\varnothing$) (Tinoco and Coco, 2018;Yang et al., 2016; Tinoco and Coco, 2016). Therefore, ripple formation may occur earlier.

Determining ripple dimensions is crucial for predicting C_0 over rippled beds (Nielsen, 1986; Nielsen, 1992; Sleath, 1991; van Rijn, 2007a; b). A modified Shields parameter for rippled beds, θ_r was presented by Nielsen (1986), who implemented Du Toit and Sleath (1981) maximum near-bed velocity over the rippled bed solution into the existing Shields parameter.

$$\theta_r = \frac{\theta'}{\left(1 - \frac{\pi\eta_r}{\lambda_r}\right)^2} \tag{4}$$

Several predictors have been developed to determine η_r and λ_r (Nielsen, 1986; Soulsby and Whitehouse, 2005; Godstein et al., 2013). In all cases, $U_{bed} > U_{thresh}$ was ensured before applying these predictors.

In this paper, the ripple dimensions are predicted using the Soulsby and Whitehouse (2005) predictor for ripple length and height, which is given as

$$\frac{\lambda_r}{A_w} = \left[1 + (1.87 \times 10^{-3})\frac{A_w}{D_{50}}\left(1 - e^{\left\{-\left(2.0 \times 10^{-4}\left(\frac{A_w}{D_{50}}\right)\right)^{1.5}\right\}}\right)\right]^{-1} \tag{5}$$

$$\frac{\eta_r}{\lambda_r} = 0.15\left[1 - e^{\left\{-\left(5000\left(\frac{D_{50}}{A_w}\right)\right)^{3.5}\right\}}\right] \tag{6}$$

Nielsen's (1986) method is commonly used to estimate reference sediment concentration, C_0. This equation was selected in this study for two reasons: firstly, the method was derived for use, especially on rippled beds. Secondly, several studies have highlighted the strength and applicability of the equation (Green and Black, 1999; Thorne et al., 2002; Goldstein et al., 2013). C_0 is defined as

$$C_0 = \gamma\rho_s\theta_r^3 \tag{7}$$

where γ, is a calibrated coefficient ranging from 0.0022 to 0.005 (Nielsen, 1986; Thorne et al., 2002).

Thorne et al. (2009) studied the impact of ripples on sediment diffusivity (ε_s) over sandy rippled beds. They discovered that vortices over rippled beds contribute to diffusivity to a height of 3 to 4 η_r. Above this region, sediment diffusivity shows a linear trend, which can be determined by

$$\varepsilon_s = \frac{-w_s C_z}{\frac{dC}{dZ}} \tag{8}$$

Here w_s is the sediment settling velocity, which was calculated using the Soulsby (1997) equation for natural sands

$$w_s = \frac{\nu}{D_{50}}\left[\left(10.36^2 + 1.049D_*^3\right)^{\frac{1}{2}} - 10.36\right] \tag{9}$$

where ν is kinematic viscosity taken as 1.26×10^{-6} and D_* is the dimensionless grain size:

$$D_* = \left[\frac{g(s-1)}{\nu^2}\right]^{\frac{1}{3}} D_{50} \tag{10}$$

These formulations and parameters serve as the baseline for presenting and discussing the results in this paper.

3. Methodology

This section describes the experimental and analytical methods used to investigate the hydrodynamic and sediment resuspension dynamics within flexible vegetation canopies. The flume facility, wave generation, and baseline instrumentation follow Ions et al. (2025) and are summarised here for completeness. All modifications specific to flexible vegetation and additional processing steps are described in full below to ensure reproducibility.

3.1. Flume and wave conditions

The experiments were conducted in a 30.7m long, 0.8m wide, and 1.2 m deep wave flume in the Coastal Engineering Laboratory of Swansea University, UK. The flume features a piston-type wave generator with both regular and random wave generation, glass sidewalls, and a metal bottom. A parabolic wave absorber, made of reticulated foam, is located at the opposite end of the wave generator (Fig. 2).

The key hydrodynamic parameters include wave period, T; significant wave height, H_s and water depth h. In our experiments H_s varied from 0.06 m to 0.2 m, and T between 1.0 s and 2.0 s, which are within the range of natural conditions (Table 1). Two water depths represented emergent ($h/h_v \leq 1$) and submerged ($h/h_v > 1$) vegetation conditions. Since the study investigates sediment suspension, the wave heights and wave periods were selected to give a range of U_{bed} values, which exceeded the threshold of motions.

In total, 85 cases are considered across the present study and Ions et al. (2025), as shown in Table 1.

3.2. Vegetation mimics

The flexible vegetation mimics used in this study were made from

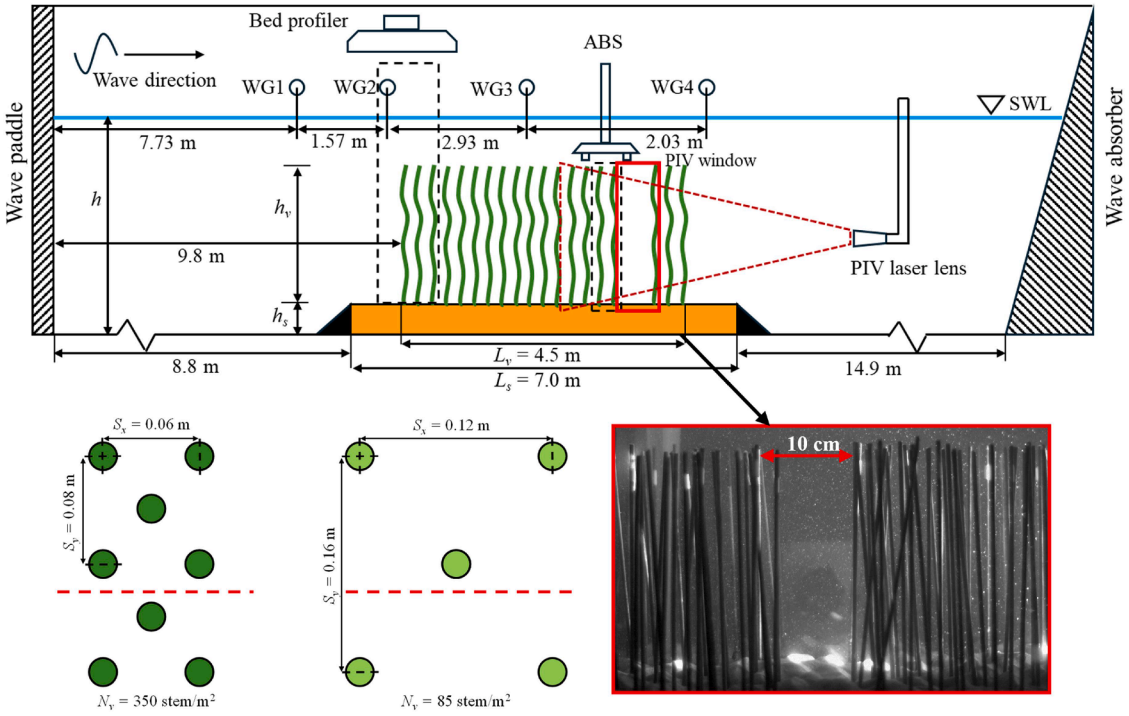

Fig. 2. Experimental setup in the 30.7 m wave flume at Swansea University. The top figure shows the flume configuration with a wave generator and vegetation canopy. The bottom figure illustrates dense and sparse vegetation stem arrangements, with red dashed lines indicating the transect used for PIV (Particle Image Velocimetry) laser measurements. Where WG1-WG4 are the wave gauges, ABS is the acoustic backscatter sensor.

silicon sealants (ρ_v = 998 kg/m^3). The rigid vegetation mimics used in Ions et al. (2025) were made from rigid bamboo dowels (ρ_v = 350 kg/m^3). The stems differed in flexural rigidity, with flexible stems measured at $EI = 1.7 \pm 0.3\ 10^{-2} Nm^2$ and rigid stems at $EI = 9.0 \pm 4\ 10^{-2} Nm^2$ calculated by van Veelen et al., 2020, who used identical vegetation mimics and plant flexural rigidities were obtained via three-point bending tests. Both types of stems had a cylindrical cross-section and the same dimensions of $b_v = 5mm$, N_v= 85 and 350 and h_v= 300 mm The two vegetation densities selected correspond to the frontal areas of ah = 0.106 and 0.61, or stem solid volume fraction ∅ =0.7% and ∅ =0.17%. These values are representative of dense and sparse array densities ($ah \langle 0.1$ for sparse arrays and $ah \rangle 0.1$ for dense arrays Nepf, 2012).

A vegetation canopy of length 4.5 m was formed by attaching nine metal sheets to the flume bottom. This included a 10 cm vegetation-free PIV window, located at 4.2 m from the start of the patch. A PIV window of 20 cm has shown to be representative of conditions within the stem array (Tseng and Tinoco, 2021; van Veelen et al., 2020). This window was used for hydrodynamic measurements to avoid disturbance from swaying flexible plant mimics. The plates covered the full width of the flume. The length of the vegetation canopy was selected to be larger than the largest wavelength used in the experiments ($\lambda_w = 3.44m$). The two N_v values 85 and 350 /m^2, represented the lower and upper bound tested, labelled as 'sparse' and 'dense' vegetation cases, respectively. Whilst denser canopies exist in nature, this range was selected to focus on conditions where ripple formation remains possible. The stem spacing, S_x, was selected to give a range of A_w/S_x, to compare the results and dependency of stem-induced processes observed within flexible vegetation canopies to previous studies through rigid vegetation canopies, in Ions et al. (2025).

The experiments ensured replication of the conditions found in nature through the consideration of the following non-dimensional parameters (Ghisalberti and Nepf, 2002; Luhar and Nepf, 2016; Luhar et al., 2017; Tang et al., 2019; van Veelen et al., 2020; Bradley and Houser, 2009; Abdelrhman, 2007): kh (ratio of water depth to wavelength); h/h_v (ratio of vegetation to water depth); H/h (ratio of wave height to water depth); Froude number, $Fr = U_w/\sqrt{(gh)}$; the vegetation Reynolds number, $Re = U_w b_v/\nu$, and Keulegan-Carpenter, $KC = U_w T/b_v$, which is a predictor for drag coefficients of cylinders. The full list of conditions found in nature and used in this study is given in Table 1.

The dynamics of flexible vegetation were characterised using two additional non-dimensional parameters: (i) the Cauchy number, Ca, which is the ratio of drag force over the restoring force of stiffness; and (ii) relative stem length, Lc, which is the ratio of stem height to wave excursion (Luhar and Nepf, 2016). These are expressed as:

$$Ca = \frac{\left(C_D\ \rho\ b_v\ U_w^2 h_v^{\ 3}\right)}{(EI)} \tag{11}$$

$$Lc\ =\ \frac{h_v}{A_w} \tag{12}$$

in which $I = \pi b_v^4/64$ is the second moment of area for the stem cross-section and C_D is the drag coefficient of the stem. For rigid vegetation ($Ca << 1$), the drag associated with the wave force is negligible relative to stem stiffness, and vegetation remains upright. For flexible vegetation, $Ca = O(1)$, stem reconfiguration occurs (Luhar and Nepf, 2016). When $Lc << 1$, the stem orientation can resemble stem movement under unidirectional steady flow (Luhar et al., 2017; van Veelen et al., 2021). When $Lc >> 1$, the stem will remain largely upright, subject only to gentle oscillations at the tip. In the present study, flexible vegetation was observed to bend fully in the direction of wave propagation for larger orbital excursions. The resulting EI and Ca ranges (Table 1) are representative of seagrass and flexible salt marsh species (Table 1; Luhar and Nepf, 2016; van Veelen et al., 2020; Hansen and Reidenbach, 2012). A description of the primary vegetation parameters considered is provided in Table 1.

Flexible vegetation mimics used in this study were also designed to bend along their full length, from the base at the sediment bed to the stem tip, in response to wave action. This expands upon the existing

Table 1
A comparison of vegetation properties and hydrodynamics in nature and in the experiments. References for the ranges observed in nature are provided in the table. The range of selected values in nature covers seagrasses, salt marshes, and mangroves.

Parameter	Ranges observed in nature	This study – Flexible mimics	Ions et al. (2025) – Rigid mimics	Units
H (wave height)	0.05 – 0.8 [1,2,3]	0.05 – 0.2	0.05 – 0.2	m
T (wave period)	1 – 8 [1,2,3]	1 – 2	1 – 2	s
h (water depth)	0 – 5 [1,4]	0.3 and 0.45	0.3 – 0.45	m
b_v (stem diameter)	2.3 – 8 [5–8]	5	5	mm
N_v (stem density)	33 – 3000 [5,9,10,11]	85 – 350	85 – 350	stems/ m^2
h_v (stem length)	0.1 – 0.6 [5,6,7]	0.3	0.3	m
E (Young's modulus)	139 – 2343 [7,12,13]	0.56	2917	MPa
EI (flexural rigidity)		$1.7 \times 10^{-5} \pm 0.5$ [25]	$9 \times 10^{-2} \pm 4$ [25]	N m^2
Seagrass	$7.5 \times 10^{-8} - 1.7 \times 10^{-5}$ [14–20]	—	—	N m^2
Salt marsh	$1.9 \times 10^{-5} - 6.6 \times 10^{-3}$ [7,8,12,13,25]	—	—	N m^2
Ca (Cauchy number)	0.04 – 80,000 [7,12]	6.22 – 2201	0.004 – 0.146	—
L_c (relative stem length)	0.5 – 12.4 [5,7]	1.5 – 12	1.5 – 12	—

References: [1] Fonseca & Cahalan (1992); [2] Infantes et al. (2012); [3] Reidenbach & Thomas (2018); [4] Koch et al. (2009) Environ. [5] Duarte (1991); [6] den Hartog (1970); [7] Rupprecht et al. (2017) [8] Boström et al. (2014)[9] Feagin et al. (2011); [10] Liu & Pennings (2019); [11] Rupprecht et al. (2015);[12] Schulze et al. (2022); [13] Keimer et al. (2021) [14] Paul et al.(2022; [15] Fonseca et al. (2019); [16] Paul & de los Santos (2019); [17] Folkard (2005); [18] Luhar, Infantes & Nepf (2017); [19] Lei & Nepf (2019); [20] Luhar & Nepf (2011); [21] Abdolahpour et al. (2017); [22] Méndez-Alonzo et al. (2015); [23] Hill et al.(2024); [24] Mori et al. (2022); [25] van Veelen et al. (2020).

literature for rigid vegetation mimics (Tinoco and Coco, 2018; Tseng and Tinoco, 2021; Ions et al., 2025). The flexible stems also differ from those previously used in experimental studies on sediment suspension in flexible vegetation studies, which often include a rigid sheath, with flexible blade mimics attached to the rigid lower portion of the stem (Zhang and Nepf et al., 2019; Ros et al., 2014). Whilst a wide range of plant flexural rigidity exists in nature, this study aimed to isolate and investigate the impact of plant swaying on bed formations and sediment suspension. Therefore, a stem that swayed directly from the base to the tip was selected.

3.3. Sediment & bed preparation

The sediment grain size distribution was $D_{50} = 300\ \mu m$, $D_{90} = 398\ \mu m$, D_{10}=160 μm and ρ_s =2.64 $g/cm3$ These values are representative of sediment found in seagrass beds and the fringes of salt marshes and mangrove forests (Masselink and Jones, 2023; Mullarney et al., 2017) and closely align with previous studies on vegetated and bare sediment bed dynamics (Marin Diaz et al., 2020; Tinoco and Coco, 2018; Thorne et al., 2002). Sediment mobility was scaled to ensure that sediment initiation could be achieved under experimental conditions.

A 5 cm layer of sediment was placed over the vegetation canopy. The total length of the sediment layer, which extended 1 m beyond the vegetation canopy on either side, was 6.5 m. The extended bare sediment bed area represented natural sediment bed conditions without vegetation, where waves often propagate over bare sediment bed regions before interacting with vegetation. To ensure the sediment was kept in the desired location, two 1/20 metal slopes were secured to the flume bottom at both ends of the sediment layer.

3.4. Instrumentation & data acquisition

Four resistance-type wave gauges ($\pm = 0.5mm$) were deployed (WG1- WG4) to record surface water elevation time series along the flume: WG1 at the toe of the slope, WG2 at the leading edge of the vegetation canopy, WG3 midway through the vegetation canopy, and WG4 immediately downstream of the vegetation canopy (Fig. 2).

Water particle velocities were measured using Particle Imagery Velocimetry (PIV) (Dantec System - Nano L 100–50, Litron Laser), at approximately 4.2 m downstream of the leading edge of the vegetation canopy. Polyamide seeding particles ($D_{50} = 50\ \mu m$) were used. Adopting established methods found in literature (e.g., Luhar et al., 2010; Pujol et al., 2013; Van Veelen et al., 2020; Tseng and Tinoco, 2021), several rows of vegetation were removed, creating a 10 cm measurement window (Fig. 2). Velocity measured within the gap have been shown to be representative of the velocity in the stem array (e.g. Tseng and Tinoco, 2021; van Veelen et al., 2020).

The PIV laser, centred at the midline of the flume, was directed downstream, with the exact location in the water column optimised for each water depth. The PIV laser was coupled with a high-speed camera at the lateral side of the flume. PIV images were captured at a rate of 50 Hz, for 45 s, corresponding to between 45 and 22 wave cycles.

The image processing and cross correlation were performed in PIV-Lab (Thielicke and Sonntag, 2021), using Contrast Limited Adjustment Histogram Equalisation (CLAHE, 20px) and an image calibration factor of 1 px = 0.00064 m. The Fast Fourier Transformation PIV settings were selected with four consecutive 50% size passes with 50% overlapped integration areas.

Stem motion occasionally introduced laser interference, and vegetation containing visible stem laser cross-over were removed from processing. The measurement transects were placed within 1 cm of the last row of vegetation before the PIV window to capture the representative flow, whilst the flow field.

The PIV-derived velocity magnitudes include a 2D velocity vector field separated into instantaneous horizontal and vertical velocity components, U_i (x, z, t), and vertical, W_i (x, z, t), respectively. Each velocity component may be decomposed into three parts. U_i can be written as

$$U(z,t) = \overline{U}(z) + \widetilde{U}(z,\varphi) + u'(z,t) \tag{13}$$

in which $\overline{U}(z)$ is the time-averaged mean current, $\widetilde{U}(z,\varphi)$ is the phase-resolved wave orbital velocity, and $u'(z,t)$is the turbulent fluctuation. The same decomposition applies to the vertical component. The mean current for each depth interval was calculated by averaging the velocity over all wave periods, such that

$$U(z) = \frac{1}{2\pi}\int_0^{2\pi} U_i(z,\varphi)d\varphi, \tag{14}$$

$U_i(z,\varphi)$ is the phase-dependent instantaneous velocity. Phase averaging followed Tinoco & Coco (2018), where $\theta \in [0, 2\pi]$is the phase average over all wave periods, computed using $N = f_s T$ phase bins of width $\delta\theta = 2\pi/N$, with $f_s = 50$Hz.The RMS wave velocity at each depth,$U_{w,rms}(z)$ was computed as the root mean square of the difference between $U_i(\varphi)$ and U. The RMS deviation of the phase-averaged velocity from the mean current was integrated over the full wave cycle as follows

$$U_{w,rms}(z) = \sqrt{\frac{1}{2\pi}\int_0^{2\pi} (U_i(z,\varphi) - U(z))^2 d\varphi} \tag{15}$$ and the two-component

turbulent kinetic energy (TKE) was computed as

$$TKE(z) = \frac{1}{4\pi}\int_0^{2\pi}\left[2u'_{rms}(z,\varphi)^2 + w'_{rms}(z,\varphi)^2\right]d\varphi \quad (16)$$

where $u'_{rms}(z,\varphi)$and $v'_{rms}(z,\varphi)$are the RMS turbulent fluctuations in the horizontal and vertical directions within each phase bin, following Tseng and Tinoco (2021, 2022).

SSC profiles were recorded simultaneously with the PIV velocity measurements using a four-frequency Acoustic Back Scatter Sensor (ABS; 0.5, 1.0, 2.0, and 4.0 MHz). The sensors were clustered with a 5 cm circumference and located just upstream of the PIV window within the vegetation canopy to capture the sediment dynamics representative of the flow field. Measurements were taken at a resolution of 2.5 mm depth intervals and a sampling frequency of 100 Hz.

Post-processing was performed using the AQUAscat MATLAB toolkit. The SSC profiles from each transducer were time-averaged and ensemble-averaged across all four sensors to obtain the final vertical SSC profile. The ABS also identified the bed location, allowing the derivation of the reference concentration C_0, at a reference elevation (Z_{ref}) above the bed, following the procedure given in Green & Black (1999). The bed location was identified as follows: $\log_{10}SSC$ was plotted against the corresponding Z value, and the break-in slope was identified by fitting a straight line to the data. The break-in slope was then taken as reference, Z_{ref}. This was repeated for all cases to obtain the mean and uncertainty in all SSC and C_0 values. The error taken was the largest difference between experimental repeats and $Zref - 1$ *and* $Zref + 1$. Further details of the calibration and inversion are provided in Ions et al. (2025).

A seabed profiler (HR-Wallingford HRBP-1070; ± 0.5 mm, 25 Hz) was mounted on top of the wave flume (Fig. 2) and deployed for selected cases, which span the range of submergence and A_w/S_x tested in Table 2. The bed morphology was measured over a region 1 m upstream and downstream of the vegetation's leading edge. These measurements were taken only to compare the interaction between vegetation and ripple development qualitatively.

Between tests, the bed was re-levelled using a pressurised hosepipe to remove residual ripples, providing a known flat initial condition for each new wave condition. Each test comprised: (i) 15 min of wave forcing (equal to 450 – 900 induvial waves depending on the conditions) to develop bedforms from the flat bed rather than waiting for full morphodynamic equilibrium, which for orbital ripples on medium sand can require timescales exceeding one hour (Soulsby and Whitehouse, 2005), this duration was selected to produce a consistent, developed ripple field reproducible across cases; (ii) waves were then stopped and the water level and suspended sediment were allowed to settle over a 20-minute period, confirmed by ABS measurements returning to no-wave baseline values; (iii) identical wave conditions were then applied three times consecutively for 40 s each, without disturbing the bed between repeats, during which water surface elevation, particle velocities, and suspended sediment concentration were recorded simultaneously. Since the bed was not re-levelled between the three consecutive runs, all three measure the same developed ripple field. The mean variation in C_0 of 20.1% between repeats, therefore, reflects the natural physical variability in near-bed sediment concentration sampled over the 78 cm^2 ABS measurement window.

Table 2
The configuration of each criterion used in Fig. 5–Fig. 12.

Category	Representative case
Emergent Wave Conditions for $\mathbf{A_w}$ /$\mathbf{S_x}$ > 0.5	B14-B17, DV14-DV17, SV14-SV17
Emergent Wave Conditions for $\mathbf{A_w}$ /$\mathbf{S_x}$ < 0.5	B10-B13, DV10-DV13, SV10-SV13
Submerged Wave Conditions for $\mathbf{A_w}$ /$\mathbf{S_x}$ > 0.5	B5-B8, DV5-DV8, SV5-SV8
Submerged Wave Conditions for $\mathbf{A_w}$ /$\mathbf{S_x}$ < 0.5	B1-B4, DV1 -DV4, SV1-SV4

3.5. Categorisation of experimental runs for analysis

The experimental cases in this study expand on the previous dataset of Ions et al. (2025). The full description of the test cases can be found in Table A1, where the new cases in this study are the flexible vegetation scenarios F-DV and F-SV, totalling 34 new cases.

To facilitate direct comparison between flexible and rigid vegetation, all experimental cases were classified into categories according to two parameters, A_w/S_x and submergence ratio. $A_w/S_x$was selected following the framework established by previous authors (Zhang and Nepf, 2019; Ions et al., 2025) in which A_w/S_x governed TKE production and the ripple development within rigid vegetated beds. Whist derived for rigid vegetation, the threshold allows direct comparison between cases, and to test the prevalence of use for flexible vegetation. Each category includes bare-bed reference cases (denoted B) and vegetated cases with dense test cases (DV), $N_v = 350$ and sparse test cases (SV), $N_v = 85$. The entire list of test case identifiers can be found in Table A1**.** The four categories and the corresponding test cases are provided in Table 2**.** This reduces the need for detailed vegetation characterisation in sediment transport models and supports the development of simplified, physically grounded parameterisations for wave-driven sediment dynamics in vegetated environments.

4. Results and discussion

The section begins with the observed motion of flexible vegetation and the formation of ripples. The resulting hydrodynamic and suspended sediment concentrations are then presented. Vegetation-flow-sediment interactions and ripple formation are then compared to those in rigid vegetation.

4.1. Wave-induced vegetation movement

Stem motion influences the flow field within vegetation canopies, as wave-induced stem movement alters the local flow dynamics (van Veelen et al., 2020; Dalrymple et al., 1984; Lowe et al., 2005). These changes alter near-bed sediment stresses and sediment entrainment, thereby increasing the complexity of sediment dynamics.

Across all flexible vegetation cases, the vegetation exhibited wave-driven motion. The stem deformation extended directly from the base of the stem (Fig. 3). The degree of stem reconfiguration across all flexible vegetation cases is quantified by Ca = 6.22–2201 and Lc = 1.5–12 (Table 1). For all flexible stem cases, Ca >> 1, confirming that hydrodynamic drag dominates over stem stiffness (Lei and Nepf, 2019), producing substantial reconfiguration under all wave conditions tested. The range of Lc indicates that stems experienced significant bending across the full range of orbital excursions. For lower Lc (≈1.5), stem deflection patterns are comparable to those under steady unidirectional flow, whilst at higher Lc (≈12), bending is concentrated progressively toward the stem tip. For the largest A_w cases, Ca > 1000 and stems were observed to flatten completely during forward wave propagation, recovering to near-vertical at flow reversal (Fig. 3). This asymmetric movement is consistent with previous observations, linking vertical velocity components to enhanced downward loading on flexible vegetation (Gijon Mancheno, 2016; Lei and Nepf, 2019). This contrasts with the rigid vegetation cases from Ions et al. (2025), where Ca = 0.004–0.146 throughout, confirming stems remained effectively upright under all conditions, maintaining a large relative displacement between stems and wave motion.

4.2. Observations of ripple formation in flexible vegetation canopies

Visual observation and bed-profiler measurements confirm formation of ripples on the vegetated sediment bed with flexible vegetation canopies in all experimental cases, with only a few exceptions. In those few cases where ripples did not form, the bed remained flat due to

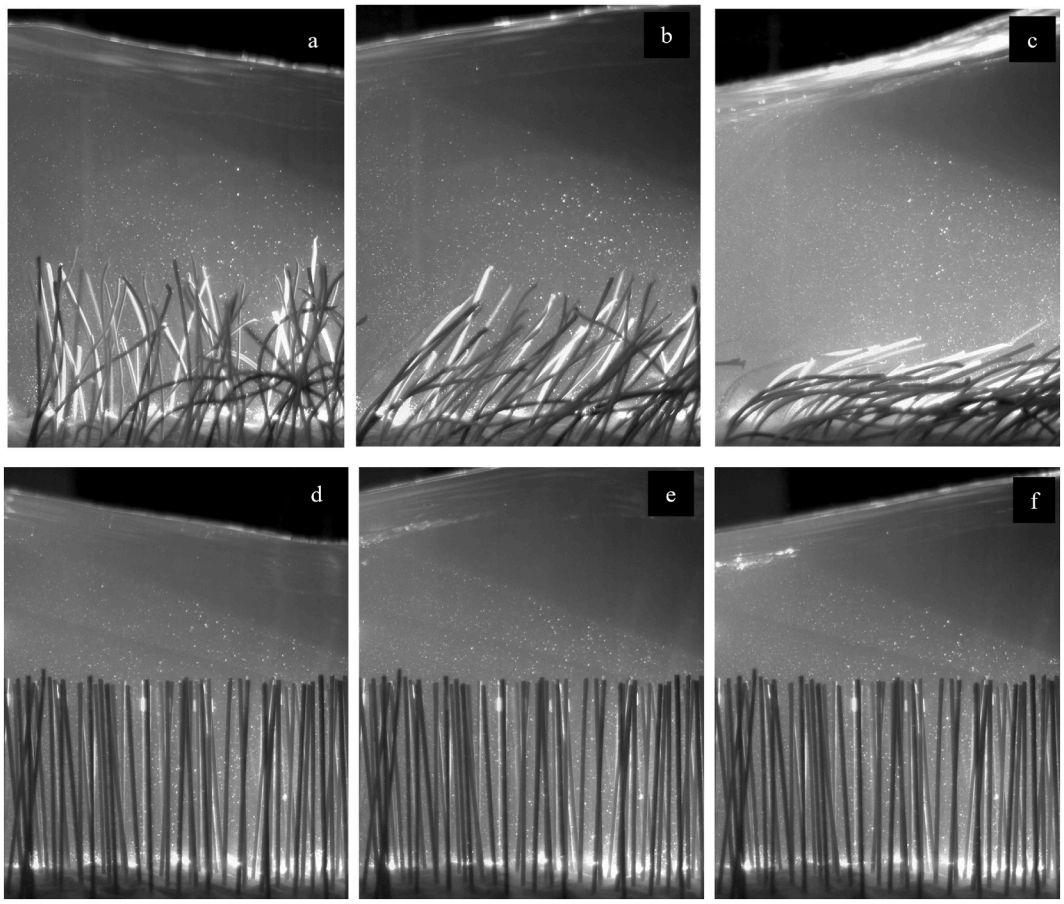

Fig. 3. PIV snapshots comparing flexible (panel a - c) and rigid (panel d-f) dense vegetation canopies under DV7 wave conditions. Both images correspond to the same phase within a wave cycle, illustrating differences in stem motion and flow structure.

$U_{bed} \leq U_{thresh}$. These cases are denoted by an Asterix in Table A1. Therefore, only the cases with ripple formation are considered in this section. Fig. 4 shows ripples in flexible vegetation canopies under a range of A_w/S_x values, to explore the role of potential stem-wake interactions with the ripple structure. Under identical wave conditions ripple structure is compared with ripples formed in rigid vegetation canopies. The region of unvegetated bed (marked dashed line) is used as a comparison of ripple structure within and outside the vegetated beds.

Ripple geometry was measured and quantified at a horizontal transect taken every 50 mm along axis 2 of the rippled bed (Fig. 4). For each transect, η_r and λ_r were determined from crest–trough and crest–crest spacing, respectively, and subsequently averaged across all transects within each region. Statistics are reported as mean ± standard deviation, representing spatial variability across detected ripples for each experimental case (Table 3).

Within the flexible vegetation canopies, scouring around individual stems and the removal of sediment from stem wakes are rarely observed, when compared to rigid vegetation canopies, under the same conditions (Fig. 4). Ripples within the flexible vegetation canopy and the bare sediment bed region remain similar when considering the dimension and structure of the average ripple profiles before and after the red dashed line (Fig. 4, Table 3). It is evident that within the flexible vegetation canopies (to the right of red dashed line), ripple crest height and length remain largely similar across most cases in Fig. 4. A two-sample t-test was used to assess differences in mean ripple dimensions (η_r, λ_r) between flexible and rigid vegetation, where each of the $n = 8$ cases provides one independent mean value, with statistical significance defined as $p < 0.05$. Results indicate that flexible vegetation shows non-significant differences ($p > 0.05$). The combined visual evidence (Fig. 4) and ripple dimension data in Table 3 therefore imply that flexible vegetation does not consistently disrupt ripple structure or organisation, and ripple formation closely resembles that of bare sediment beds under the majority of conditions tested.

In contrast, rigid vegetation substantially alters ripple morphology. Considering the regions before and after the red dashed lines (Fig. 4), ripple crests are fragmented, with reduced heights and shorter wavelengths compared to bare-bed conditions (Fig. 4, Table 3), particularly for cases with larger A_w/S_x. Pronounced sediment removal around rigid stem bases is evident, for the cases where $A_w/S_x > 0.5$. This is consistent with enhanced local shear and wake-driven erosion. These trends are observed consistently across all wave conditions tested (Fig. 4) and are supported by statistically significant differences in ripple metrics for rigid vegetation in the majority of cases ($p < 0.05$), excluding SV7 and SV13 which were not statistically significant.

The processes which govern the removal of sediment within rigid vegetation canopies and ripple crests are primarily associated with vortex shedding around individual stems (Tinoco and Coco, 2018; Zhang and Nepf, 2019). The absence of scouring around the flexible vegetation stems suggests that for the flexible vegetation in this study, significant levels of stem vortices were not generated under most conditions tested. As a result, ripple structure is largely comparable to bare sediment beds. The preservation of ripple structure can have direct implications for near-bed TKE and sediment suspension, as discussed in the following sections.

4.3. Flow hydrodynamics over vegetated rippled beds

This section examines flow velocity within flexible vegetation can-

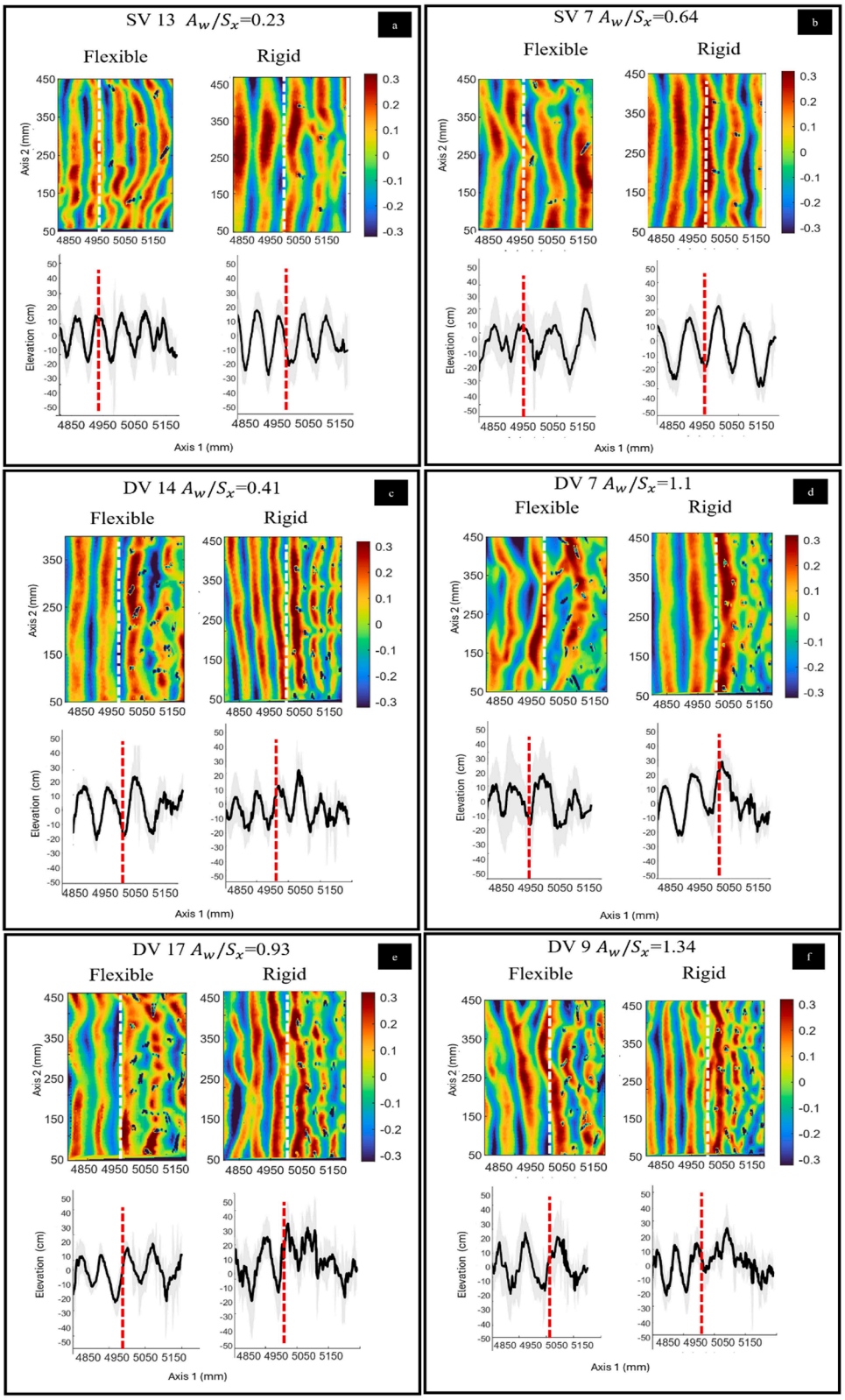

Fig. 4. Bed profile surveys for bare sediment and vegetated beds under wave forcing. In each section, the top figure shows measured bathymetry with a colour scale: red = ripple crests, blue = ripple troughs and units are centimetres. The bottom figure in each panel presents cross-sectional profiles averaged every 50 mm along axis 2, with ±1 standard deviation indicated. Black circles mark stem positions; wave propagation is from left to right. A region of unvegetated sediment bed is shown to the left side of each figure, for comparison within the vegetated sections, marked by dashed vertical lines.

Table 3
Quantification of ripple geometry associated with the rippled beds shown in Fig. 4. The table provides the mean ripple crest height η_r and ripple wavelength, λ_r, averaged across all horizontal transects ($\Delta y = 50$ mm), for regions upstream and downstream of the vegetated bed (relative to the red dashed line in Fig. 4). Values are reported as mean ± standard deviation, representing spatial variability across detected ripples within each region.

	Average Ripple Crest Height (η_r mm)				Average Ripple Wavelength (λ_r mm)			
Case	Before 1st row of stems		After 1st row of stems		Before 1st row of stems		After 1st row of stems	
	Flexible	Rigid	Flexible	Rigid	Flexible	Rigid	Flexible	Rigid
SV7	33 ± 7	34 ± 2	34 ± 10	32 ± 7	82 ± 24	77 ± 5	84 ± 3	72 ± 6
SV13	23 ± 6	23 ± 6	24 ± 5	17 ± 2	70 ± 4	70± 4	64± 7	70 ± 2
DV7	32 ± 11	31 ± 6	28 ± 5	22 ± 4	90± 2	94± 4	91 ± 3	83 ± 9
DV14	40 ± 1	32 ± 7	31 ± 12	21 ± 4	63 ± 6	67 ± 3	75 ± 3	65 ± 2
DV9	31 ± 2	27 ± 1	27 ± 3	13 ± 3	110 ± 6	107 ± 5	98 ± 9	101 ± 1
DV17	30 ± 1	30 ± 8	29 ± 1	21 ± 2	62 ± 12	66 ± 4	69 ± 7	71 ± 6

opies and compares them with those in rigid vegetation canopies under the same test conditions, as shown in Ions et al. (2025). The comparisons provided in Fig. 5–Fig. 7 between flexible and rigid vegetation were grouped according to A_w/S_x and submergence ratio (Section 3.5). For each group, a moving average was applied to the profiles to obtain a mean profile, and the standard deviation was calculated.

4.3.1. Velocity measurements

In flexible vegetation canopies for emergent cases with $A_w/S_x > 0.5$, the velocity was attenuated in the lower stem region ($h/h_v < 0.25$), however, it remained within the measured variation of bare bed cases (Fig. 5**a**). Over the remaining stem height, the velocity was comparable to bare sediment bed cases (Fig. 5**a**). When $A_w/S_x < 0.5$ the attenuation was comparable to bare bed conditions, over the full stem height (Fig. 5**c**).

For submerged vegetation canopies, when $A_w/S_x < 0.5$, both flexible and rigid vegetation showed minimal velocity attenuation, closely resembling the bare sediment bed conditions (Fig. 5**d**). For submerged conditions, where $A_w/S_x > 0.5$, flexible vegetation attenuated the velocities, but only in the lower stem region ($h/h_v < 0.25$) (Fig. 5**b**). In contrast, rigid vegetation continued to attenuate velocity over the entire stem height (Fig. 5**b**).

This difference reflects the reduced relative motion between flexible stems and wave orbital excursion, which limits drag-induced energy dissipation (Ros et al., 2014; van Veelen et al., 2020; Zhang et al., 2018). These trends contrast with the rigid vegetation attenuation reported in Ions et al. (2025), where the velocity was reduced across the entire stem height, for both submerged and emergent conditions. Importantly, the

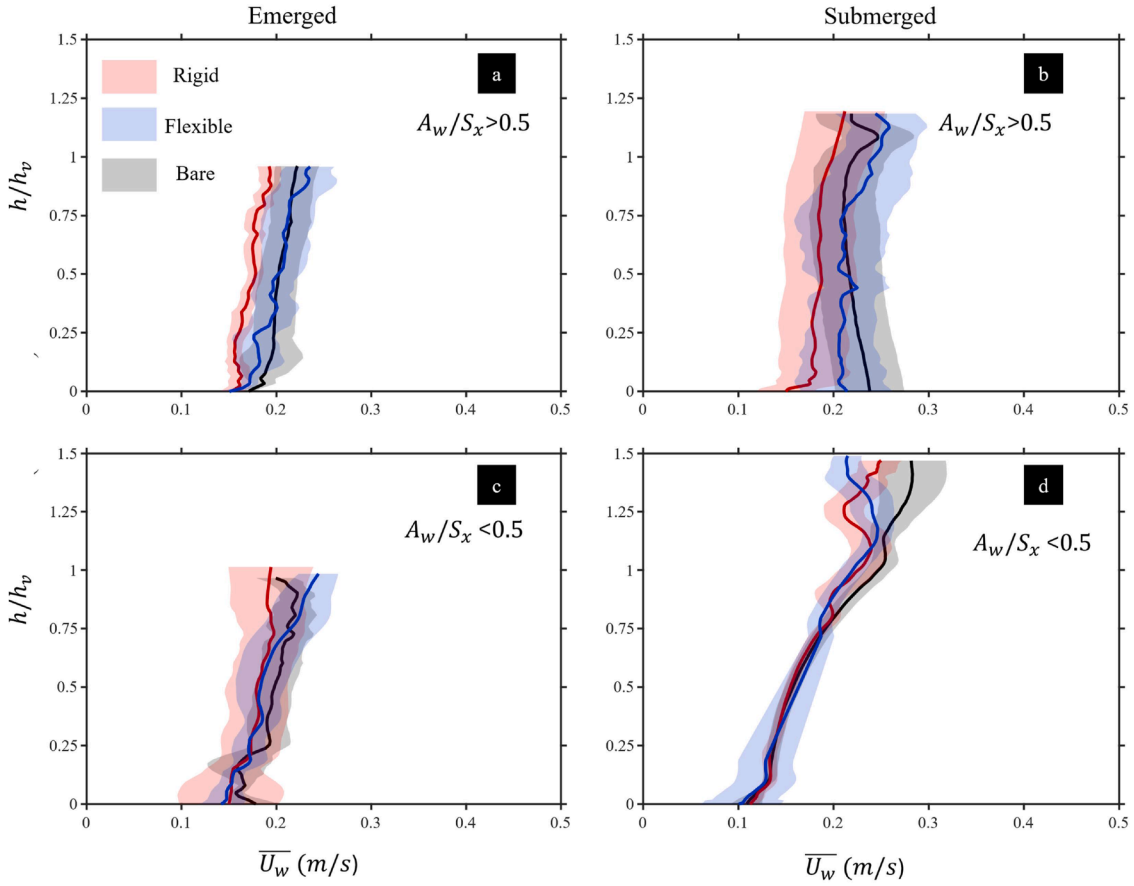

Fig. 5. Vertical profiles of time-averaged wave velocity ($\overline{U_w}$) for all test cases, at transect T1. Profiles are grouped by A_w/S_x and submergence ratio as defined in Section 3.5. Solid lines indicate mean values; shaded regions represent ±1 standard deviation. Blue = flexible vegetation, red = rigid vegetation, grey = bare sediment bed. Case groupings correspond to Table 2. In panel (b) the data above $h/h_v \sim 1.2$ is removed due to significant noise in the PIV measurements above the canopy.

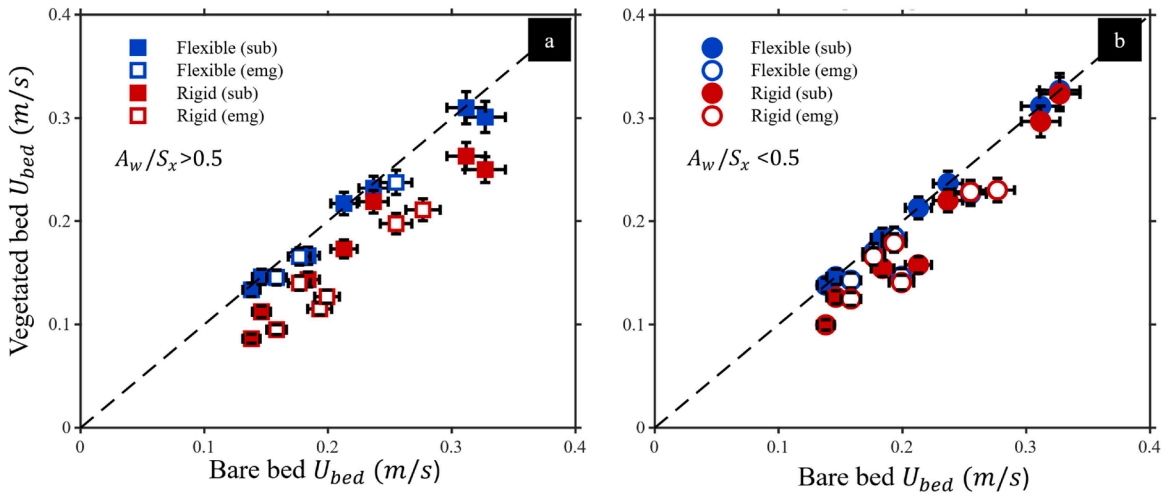

Fig. 6. Near-bed velocity (U_{bed}) for rigid and flexible vegetation canopies under two conditions: (a) $A_w/S_x > 0.5$ and (b) $A_w/S_x < 0.5$. Error bars indicate variability between repeated runs. Solid markers = submerged vegetation; hollow markers = emergent vegetation.

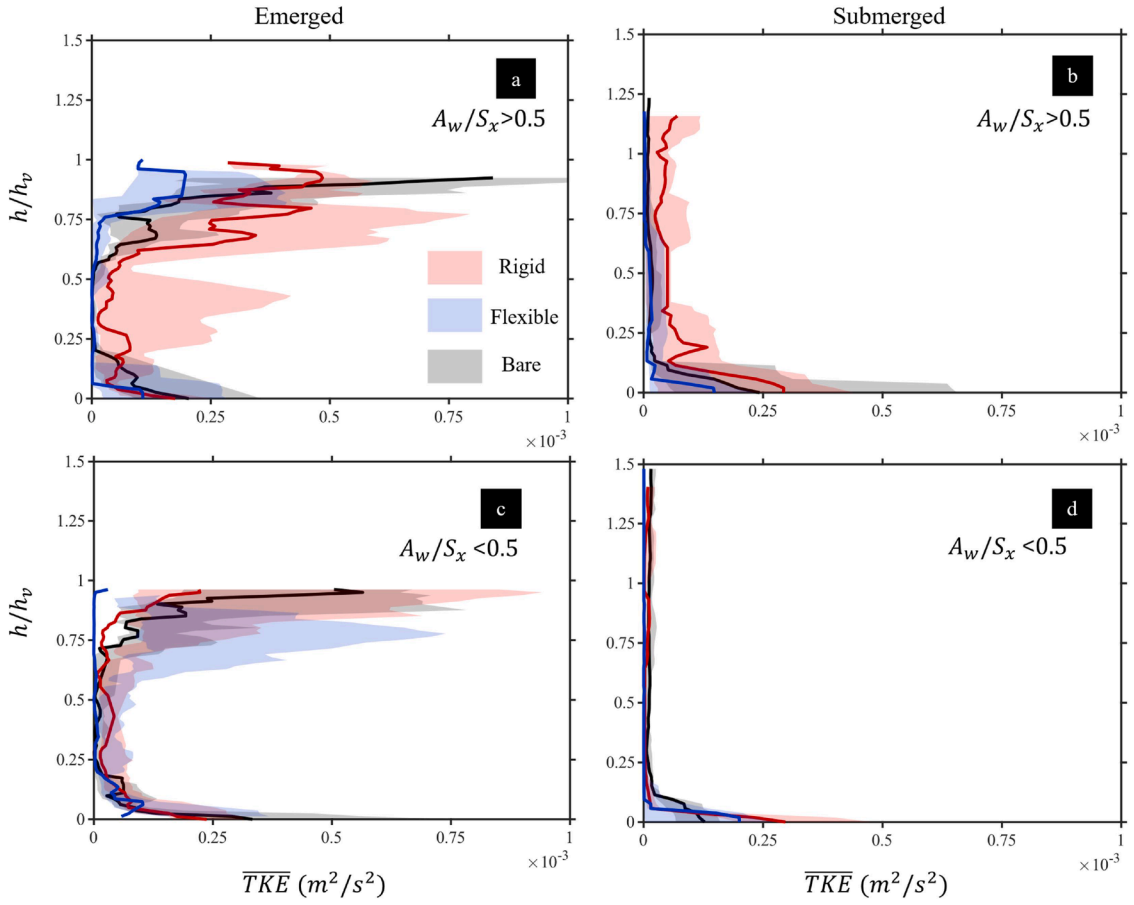

Fig. 7. Vertical profiles of wave-period-averaged turbulent kinetic energy ($\overline{TKE}$) for all test cases, at transect T1. $\overline{TKE}$ is computed by integrating over all phase bins (Eq. (14)), yielding a single depth-dependent profile per test case. Profiles are grouped by $A_w/S_x$and submergence ratio as defined in Section 3.5. Solid lines indicate mean values; shaded regions represent ±1 standard deviation. Blue = flexible vegetation, red = rigid vegetation, grey = bare sediment bed. Case groupings correspond to Table 2. In panel (b), the data above $h/h_v \sim 1.2$ is removed due to significant noise in the PIV measurements above this height.

magnitude of reduction was increased when $A_w/S_x > 0.5$ within rigid vegetation canopies. In this study, the impact of $A_w/S_x > 0.5$ does not appear to be prevalent, for the range of stem densities considered.

U_{bed} in the flexible vegetation canopies under all test conditions and their comparison with those in rigid canopies and in bare sediment bed cases are shown in Fig. 6**.** Across the full range of wave conditions, U_{bed} within the flexible canopies remained comparable to bare sediment beds. Under identical wave forcing, U_{bed} in flexible vegetation canopies is consistently higher than beneath rigid canopies and similar to bare-bed values. Notably, when A_w/S_x>0.5 flexible canopies have higher U_{bed} values (Fig. 6**a**), when compared to (A_w/S_x<0.5) rigid canopies under the same conditions (Fig. 6**b**).

Although U_{bed} is attenuated by flexible vegetation when $A_w/S_x > 0.5$, the effect is weak relative to rigid vegetation, where A_w/S_x strongly governs U_{bed} (Lowe et al., 2005; Zhang et al., 2018; Ros et al., 2014). This reinforces arguments that the swaying of vegetation substantially limits the capacity of vegetation to reduce near-bed flow velocities, which is consistent with the reduced relative motion between flexible stems and the oscillatory flow described above.

To quantify near-bed velocity attenuation, bare-bed cases under matched wave forcing were used as a baseline representing unobstructed near-bed flow. The stem-attributable velocity reduction was defined as $\Delta U = U_{bed,veg} - U_{bed,bare}$. Expressed as a percentage of the bare-bed baseline, flexible canopies produced modest and statistically non-significant reductions with median values of 0% ($p = 0.06$) and −5% ($p = 0.01$) for sparse and dense configurations respectively. For rigid canopies, velocity reductions were substantially larger and highly significant, with sparse rigid canopies reduced near-bed velocity by a median of −14% ± 9% ($p = 0.0002$), and dense rigid canopies by −23% ± 10% ($p = 0.0002$).

Rigid canopies reduced near-bed velocity more than flexible canopies, consistent with the greater wave attenuation capacity of rigid stems compared with flexible stems (van Veelen et al., 2020). For rigid canopies, emergent conditions produced greater attenuation (sparse: −15%; dense: −31%) than submerged conditions (sparse: −14%; dense: −22%). Flexible canopies showed no clear dependence on submergence state (sparse: 0% submerged, −10% emergent; dense: −2% submerged, −7% emergent), and neither case was statistically significant. These results indicate that stem rigidity and canopy density are the primary controls on near-bed velocity attenuation, with flexible canopies exerting comparatively little influence on the near-bed velocity field above that set by wave-bed interaction.

Whilst the submergence ratio is expected to directly influence the amount of wave attenuation, under scenarios where the canopy shear layer has not yet formed above the canopy, emergent and submerged conditions can behave very similarly (Lowe et al., 2005; Belcher et al., 2003); Abdolahpour et al., 2017). The formation of such a shear-layer is subject to a temporal constraint defined by the canopy-scale KC, $KC_{canopy} = \frac{UT}{L_D}$, where $L_D$is the canopy drag length scale (Belcher et al., 2003; Lowe et al., 2005). Shear-layer-driven TKE is expected only when $KC_{canopy} > 5$(Abdolahpour et al., 2017). In the present study, all submerged cases fall below this threshold, where$KC_{canopy} \cong 0.55 - 2.18$, indicating insufficient time for shear-layer growth and instability.

4.3.2. TKE measurements

Vertical TKE profiles also showed a clear difference between the flexible and rigid vegetation (Fig. 7). In flexible vegetation canopies, the TKE levels were comparable to those on the bare sediment bed over the full height of the stem and A_w/S_x did not appear to influence TKE production within the flexible vegetation canopies, for both submergence ratios (Fig. 7**a, c versus** Fig. 7**b, d**). This behaviour is consistent with the existing research, that suppression of stem-generated vortex shedding due to stem motion reduces relative stem–flow velocity (Luhar and Nepf, 2011; Ros et al., 2014; Luhar et al., 2016).

In contrast, rigid vegetation canopies, for submerged and emergent conditions, consistently enhanced TKE, above bare-bed levels, when $h/h_v > 0.15$, particularly for $A_w/S_x > 0.5$ (Fig. 7). This is consistent with increased stem-generated vortices around individual stems, enhancing stem-generated TKE in the stem region (Zhang et al., 2018; Tinoco and Coco, 2018).

The near-bed TKE values are comparable in all groups (Fig. 7) and are examined in greater detail in Fig. 8. The near-bed TKE with and without vegetation is compared to analyse the role of stem-generated TKE and ripple-generated TKE in the near-bed region. Although there is some data scatter, near-bed TKE on vegetated sediment beds are comparable to those on bare sediment beds under the conditions, irrespective of the submergence ratio and A_w/S_x, suggesting the prevalence of ripple-generated TKE. In this study, the near-bed region of flexible canopies exhibits TKE levels comparable to bare sediment bed cases (Fig. 8). This behaviour is consistent with the limited impact of flexible vegetation on bedform geometry (Fig. 4).

To separate ripple-scale and stem-scale TKE contributions, bare bed cases under matched wave forcing were used as a ripple-only TKE baseline. The stem-attributable increment was defined as $\Delta TKE = 100(TKE_{veg} - TKE_{bare})/TKE_{bare}$. Near-bed TKE in vegetated cases correlated with matched bare-bed values across all groups (R^2 =

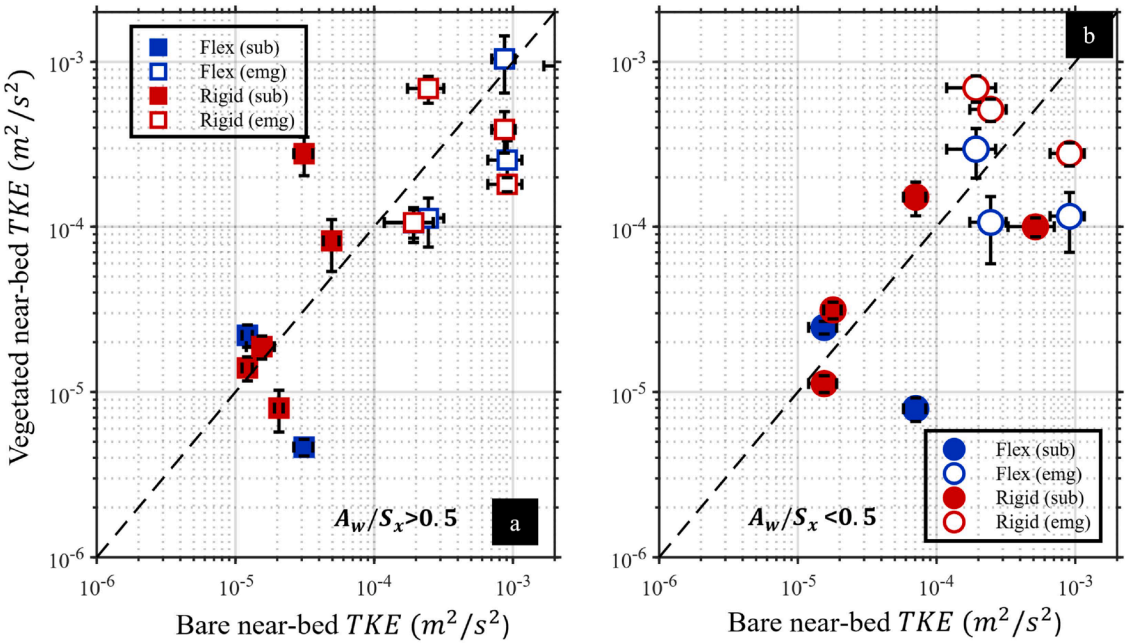

Fig. 8. Near-bed TKE for rigid and flexible vegetation canopies under two conditions: (a) $A_w/S_x > 0.5$ and (b) $A_w/S_x < 0.5$. Error bars indicate variability between repeated runs. Solid markers = submerged vegetation; hollow markers = emergent vegetation. X and Y-axis is provided in log scale to allow comparison between large and small values.

0.65–0.95), indicating that ripple geometry, driven by wave forcing conditions, is the primary determinant of near-bed TKE variance regardless of vegetation presence. Expressed as a percentage of the bare-bed baseline, median values were −11% ± 61% ($A_w/S_x > 0.5$) and −18% ± 40% ($A_w/S_x < 0.5$) for flexible canopies, indicating that stem-generated TKE did not systematically augment near-bed turbulence above ripple-induced levels. No statistically significant difference from bare-bed TKE was detected for flexible canopies ($A_w/S_x > 0.5$, p = 0.95, $A_w/S_x < 0.5$,p = 0.74).

For rigid canopies with $A_w/S_x > 0.5$, the median stem-attributable TKE increment was 31%± 37% relative to bare-bed conditions (R^2 = 0.65, p = 0.06), marginally non-significant at the 0.05 level but consistent with partial stem-wake enhancement at larger orbital excursions. For rigid canopies where $A_w/S_x < 0.5$, the median increment was −9% ± 32% (R^2 = 0.76, p = 0.70), with no detectable difference from bare-bed TKE. Across all groups, near-bed TKE in vegetated cases correlated strongly with matched bare-bed values (R^2 = 0.65–0.95), indicating that wave forcing conditions and the ripple geometry they produce, are the primary determinant of near-bed TKE variance, regardless of vegetation presence or type.

Over bare sediment beds with ripples, the primary source of near-bed TKE is vortex shedding from ripple crests (Sleath, 1995; Soulsby, 1997). Since ripple structure within flexible vegetation canopies remains spatially coherent and dimensionally comparable to bare-bed conditions (Fig. 4, Table 3), the intensity of ripple-induced vortex shedding and therefore near-bed TKE, is similarly preserved. As ripple structure within flexible vegetation canopy remains spatially coherent and comparable to that on bare beds, a similar magnitude of vortex-ripple TKE can be generated. Davies and Thorne (2008) demonstrated that vortex-shedding intensity was related to ripple steepness; therefore, comparable ripple crest height and length will generate comparable TKE levels.

Within vegetated beds where ripple structure persists, two modes of TKE generation may coexist: stem-generated turbulence and ripple-induced vortex shedding (Zhang and Nepf, 2019; Ions et al., 2025). Over flat sediment beds, stem-generated TKE is the dominant source of near-bed turbulence (Tang et al., 2019; Yang et al., 2016; Tseng et al., 2021), where no competing bedform-generated vorticity is present. However, it is not clear whether this dominance would persist when ripple-induced vortex shedding is also active. The two TKE sources operate at different spatial scales and may interact nonlinearly depending on ripple geometry, stem density, and orbital excursion.

The present results, together with studies on rippled beds occupied by rigid vegetation, indicate that near-bed TKE is primarily governed by ripple-induced vortex shedding, provided ripple geometry is maintained (Zhang and Nepf, 2019; Ions et al., 2025). While stem-scale turbulence may contribute locally in the immediate vicinity of individual stems, near-bed TKE remains comparable to bare-bed cases, indicating dominance of bedform-generated vortices. When ripple structure is substantially degraded, i.e., in dense rigid vegetation canopies, near-bed TKE can be reduced relative to bare beds and stem-generated turbulence becomes more influential (Zhang and Nepf, 2019; Ions et al., 2025). The present results suggest that this transition may occur at higher A_w/S_x thresholds or not occur for fully flexible vegetation.

Submergence ratio showed larger values of near-bed TKE production under emergent conditions (Fig. 8). This can likely be explained by larger values of A_w at the bed when the water depth is shallow which can increase ripple size and, therefore the ripple-generated TKE (Davies and Thorne, 2008). Secondly, the absence of a canopy-top vortex shedding layer which is associated with certain submerged canopies. In flexible canopies, stem pronation can further lower the position of the canopy-top shear layer, bringing TKE production closer to the bed (Abdolahpour et al., 2017), but under the present test conditions, no shear-layer is expected to form, as explained previously in the section.

4.4. Vertical sediment diffusivity profiles over vegetated rippled beds

The vertical diffusivity profiles ($\overline{\varepsilon_s}$) for each test case were calculated using a methodology similar to that described by Thorne et al. (2002) and Thorne et al. (2009). Using Eq. (8) firstly for each test case, and then a moving average was applied to $\varepsilon_s$for each of the categories defined in Section 3.5. The resultant averaged vertical diffusivity profiles and standard deviation are shown in Fig. 9. It was observed that for all wave conditions used in the experiments, suspended sediment did not extend beyond 10 cm above the bed, for the highest SSC cases. Therefore, the sediment diffusivity profiles in Fig. 9 are limited to the region between the seabed and the maximum elevation above the seabed for that group of test cases.

Across all bare sediment bed and vegetation configurations, two distinct vertical sediment diffusivity regimes are identified. The first is a near-bed, ripple-dominated diffusivity regime, associated with coherent vortex shedding from ripple crests (Thorne et al., 2002). The second regime in which diffusivity increases with height from the bed as wave orbital motion increases. The measurements in this region are also impacted as sediment concentrations decrease away from the bed. The relative structure and vertical extent of these regimes, however, vary depending on vegetation rigidity.

For bare sediment beds, the near-bed ripple-dominated regime is clearly defined and characterised by approximately uniform diffusivity over a finite vertical extent above the bed (Fig. 9**a–d**). This behaviour reflects sediment mixing driven by coherent vortices generated at ripple crests, consistent with previous observations over rippled beds (Thorne et al., 2002, 2009). Above this region, the second diffusivity regime is observed in which sediment diffusivity increases with height, consistent with the behaviour reported by Thorne et al. (2002, 2009), who attributed this increase to turbulence associated with the oscillatory wave boundary layer rather than ripple-induced vortex shedding.

Similarly, within flexible vegetation canopies, two diffusivity regimes are observed under all wave conditions, for both submerged and emergent conditions. The near-bed ripple-dominated diffusivity regime closely resembles that measured over bare sediment beds, both in magnitude and vertical extent (Fig. 9**a–d**). The height of this regime above the bed is larger under submerged conditions than under emergent conditions. The similarity between bare sediment beds and flexible vegetation reflects the impact of the preservation of ripple morphology within flexible canopies (Fig. 4). Since the intensity and vertical extents of ripple-induced vortices depend primarily on ripple height and steepness (Davies and Thorne, 2008), the maintenance of ripple geometry directly leads to preserved near-bed sediment mixing. These results demonstrate that, despite the presence of a vegetation canopy, ripple-scale processes remain the dominant control on near-bed sediment diffusivity when vegetation is flexible.

Above the ripple-dominated regime, diffusivity within flexible vegetation increases linearly with height, closely resembling bare-bed cases. There is no notable shift in this regime, which may be attributed to the diminished stem-generated vortices within flexible vegetation, which do not substantially modify the vertical structure of sediment diffusivity beyond the near-bed region.

In contrast, rigid vegetation canopies exhibit a modified two-regime structure. While a near-bed ripple-dominated diffusivity regime is still present, its vertical extent is reduced relative to both bare-bed and flexible-vegetation cases (Fig. 9**a** to **d**). This reduction is likely due to a combination of disrupted ripple morphology and enhanced sediment removal associated with velocity attenuation and stem-scale wake interactions, which may lead to a reduction in near-bed vortex shedding coherence and the vertical extents of ripple-generated vortices.

For both emergent and submerged conditions, immediately above the near-bed regime, diffusivity is slightly elevated, particularly for cases where $A_w/S_x > 0.5$ (Fig. 9**a** and **c**). This behaviour may be attributed to the decreasing dominance of ripple-induced turbulence with increasing distance from the bed, coupled with the increasing

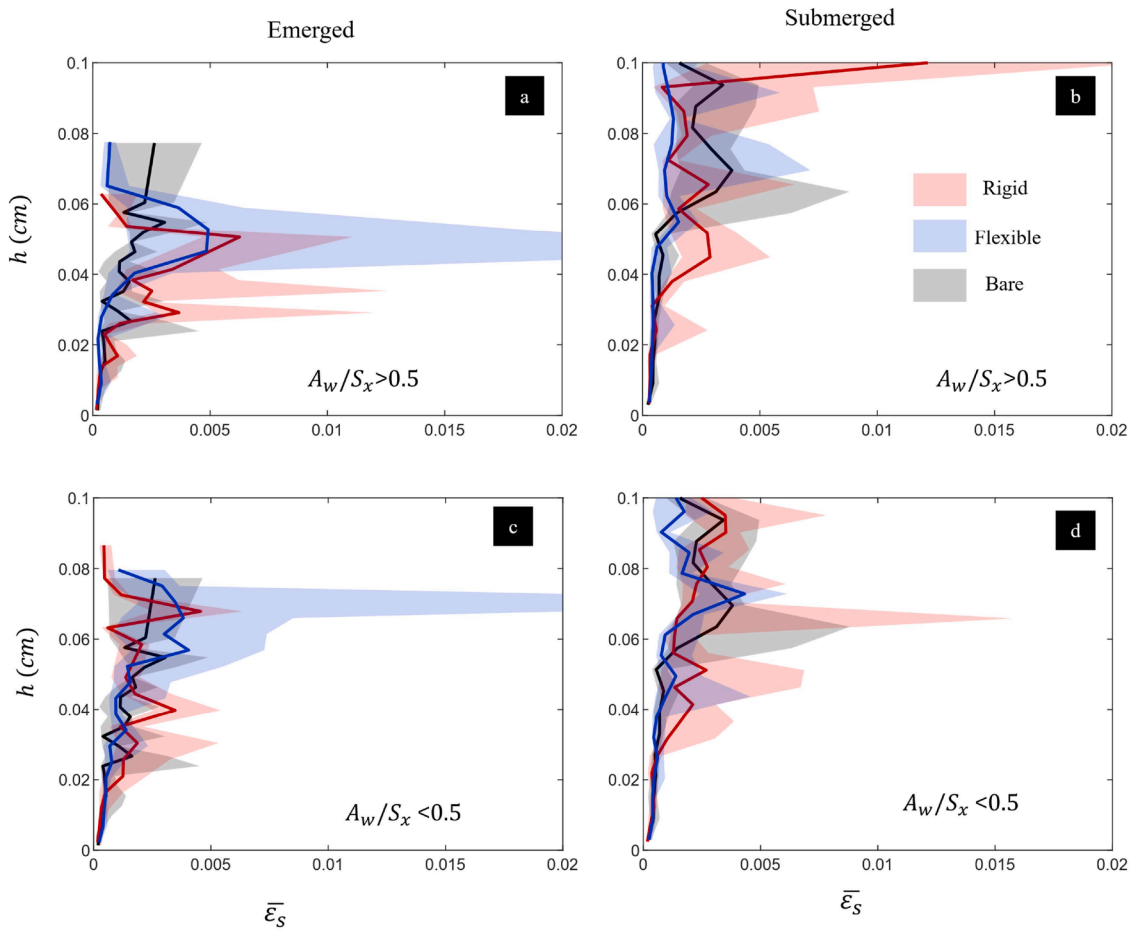

Fig. 9. Vertical profiles of sediment diffusivity ($\overline{\varepsilon_s}$), averaged according to A_w/S_w and submergence ratio, as set out in Section 3.5. Solid lines indicate mean values; shaded regions represent ±1 standard deviation. Blue = flexible vegetation, red = rigid vegetation, grey = bare sediment bed. Case groupings correspond to Table 2. Elevated standard deviation at heights further from the bed reflects low suspended sediment concentrations approaching the instrument detection limit, which amplifies uncertainty in the diffusivity estimate (Eq. (8)).

influence of stem-generated vortices higher in the water column. As ripple-scale vortices lose coherence away from the bed, stem-scale turbulence becomes progressively more relevant to sediment mixing, particularly under larger A_w farther from the bed.

Above this region, sediment diffusivity returns to levels comparable to those over bare beds. This reduction likely reflects the vertical confinement of suspended sediment, such that limited sediment availability restricts further vertical exchange, despite the continued presence of stem-generated turbulence observed within rigid vegetation canopies.

These observations demonstrate that ripple-induced vortex shedding still governs sediment mixing in the near-bed region over vegetated rippled beds, irrespective of vegetation presence or type, provided that ripple structure is preserved. Previous studies have shown that stem-generated TKE enhances sediment diffusivity over flat beds (e.g. Ros et al., 2014; Xu and Nepf, 2020). Notably, flexible vegetation preserves ripple geometry and therefore sustains ripple-induced mixing processes, whereas rigid vegetation modifies ripple structure and alters the vertical extent of the near-bed diffusivity regime.

The limited influence of vegetation-generated turbulence on sediment diffusivity above the near-bed regime can be further explained by the strong vertical confinement of suspended sediment observed in all cases (Fig. 9). Since sediment concentration gradients are strongest near the bed, vertical sediment exchange is dominated by ripple-induced vortex shedding. Turbulence generated higher in the water column, therefore has limited capacity to influence sediment mixing under the present wave conditions and sediment grain size. It is noted that finer sediments, which may remain suspended higher in the water column, could exhibit different behaviour.

These findings highlight that sediment diffusivity near the bed remains governed by ripple-scale processes when vegetation is present, and bedforms persist, despite the clear differences in canopy-scale hydrodynamics between flexible and rigid vegetation (Fig. 5–Fig. 8). Since vertical sediment diffusivity governs the efficiency with which near-bed suspended sediment is mixed upward, these results indicate that near-bed reference concentrations, C_0, may be predicted using conventional formulations over rippled beds.

4.5. *Near-bed suspended sediment concentration (C_0) over vegetated rippled beds*

Fig. 10 summarises and compares the C_0 values measured within flexible vegetation canopies, compared with rigid vegetation canopies and bare sediment beds under identical wave conditions.

In flexible vegetation, C_0 values are generally comparable to those on bare sediment beds and higher than those on rigid vegetation canopies, for both A_w/S_x>0.5 and A_w/S_x< 0.5 (Fig. 10). In rigid vegetation canopies, C_0 values are consistently lower compared to those on bare sediment bed cases, especially when A_w/S_x>0.5 (Fig. 10**a**).

These results well align with the observed velocities within flexible vegetation canopies (Fig. 5 and Fig. 6). For both vegetation types and canopy densities tested, the primary effect of the vegetation is to reduce near-bed flow velocity and limit ripple crest dimensions (Fig. 4). Flexible vegetation preserves coherent ripple geometry and maintains near-bed

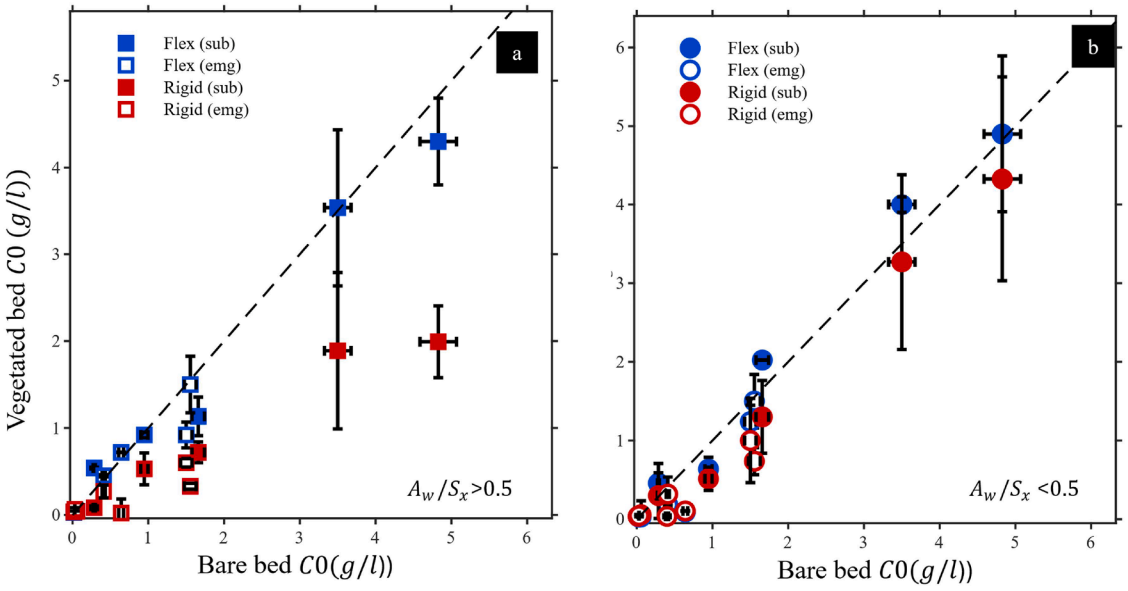

Fig. 10. Reference suspended sediment concentration C_0 in rigid and flexible vegetation canopies. (a) rigid vegetation; (b) flexible vegetation. The error bars represent the difference between C_0 values at depths Zref - 1 and Zref + 1. Solid markers = submerged vegetation; hollow markers = emergent vegetation.

velocities comparable to bare-bed conditions, resulting in higher sediment resuspension than rigid vegetation canopies.

These observations indicate that C_0 in vegetation, when ripples are present, may be governed directly by U_{bed}. In Fig. 11, the C_0 values from all experimental cases were plotted against U_{bed}. Results from both flexible and rigid vegetation canopies, stem densities and wave conditions are included in this figure. All data fall within the measured standard deviation of the fitted power law, which follows the classical format for velocity-driven SSC over rippled beds (Thorne et al., 2002;2009) and explains 97% of the variance.

Both flexible and rigid vegetation C_0 can be directly presented as a function of U_{bed}. No systematic separation by vegetation type, stem density, or rigidity is observed. Under the wave-driven conditions examined here, near-bed velocity provides the dominant control on sediment resuspension, overriding direct effects of vegetation-induced TKE.

This behaviour contrasts with previous studies of sediment transport within rigid vegetation canopies over flat beds. In those cases, sediment resuspension has been attributed primarily to stem-generated TKE, often resulting in increased reference concentrations despite reductions in U_{bed} (Ros et al., 2014; Tinoco and Coco, 2014; 2018; Tang et al., 2019; van Veelen et al., 2025). In those studies, relationships between C_0 and U_{bed} were typically identified only within individual stem-density groupings, reflecting a balance between velocity attenuation and TKE enhancement that varied with canopy configuration. In contrast, C_0–U_{bed} relationship observed here suggests that, once bedforms are present, sediment suspension is primarily controlled by ripple-induced resuspension rather than by canopy-scale TKE production.

Finally, Fig. 12 compares measured C_0 with C_0 calculated using Eqs. (2) to (7), which represent the method used over bare sandy rippled beds. The ripple dimensions are also calculated adopting the method used on bare sediment beds. Measured U_{bed} were used. The plot reveals a

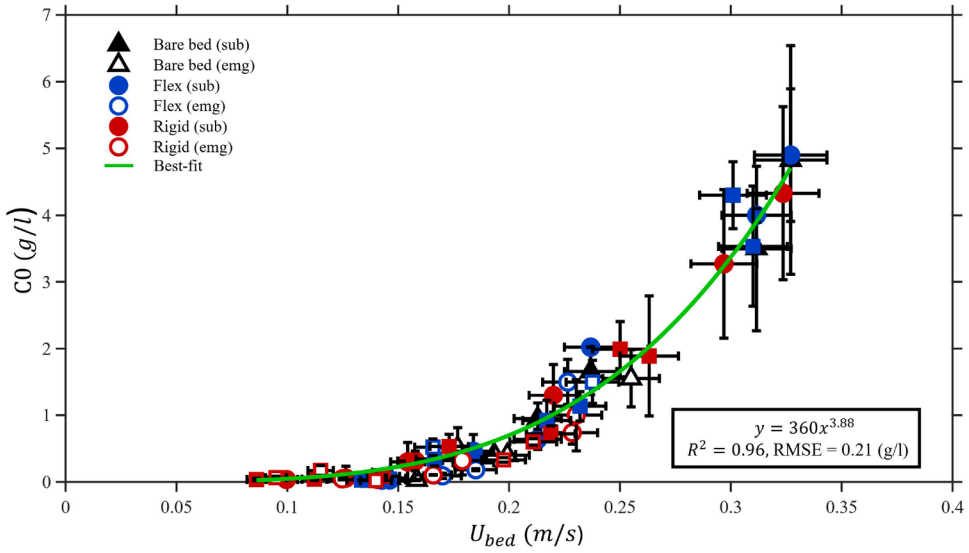

Fig. 11. Relationship between reference suspended sediment concentration (C_0) and near-bed velocity (U_{bed}) for all cases. Vertical bars represent variation between Z_{ref} and adjacent depth bins. Horizontal bars represent variation between repeat test cases. The green line indicates the best-fit power-law trend. Solid markers = submerged vegetation; hollow markers = emergent vegetation.

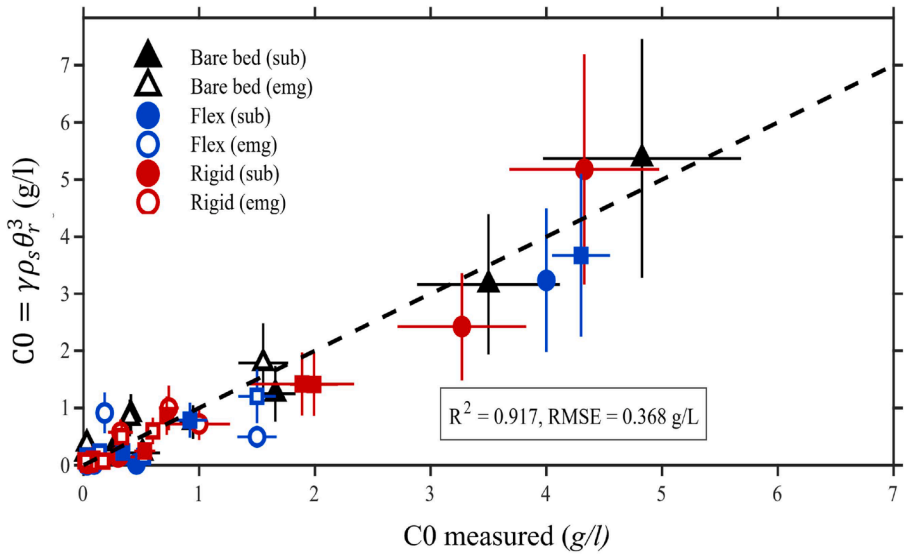

Fig. 12. Relationship between measured reference suspended sediment concentration (C_0) and calculated C_0 using Eqs. (2) to 7, for all cases. Vertical bars represent variation between coefficient in Eq. (7). Horizontal bars represent variation between repeat test cases. Solid markers = submerged vegetation; hollow markers = emergent vegetation.

good agreement between the measured and predicted C_0, using the modified shields parameter.

This behaviour emphasises the central role played by ripple-induced vortex shedding governing sediment suspension. When waves propagate over rippled beds, flow reversal generates coherent vortices that are shed from ripple crests and ejected into the water column, entraining large volumes of sediment into suspension (Nielsen, 1992; Thorne et al., 2002). Under the conditions examined here, these ripple-generated vortices dominate near-bed sediment dynamics within flexible vegetation and to a lesser extent in rigid vegetation canopies. Vegetation influences sediment suspension primarily through an attenuation of U_{bed} and thereby controlling ripple geometry and the intensity of vortex shedding.

5. Conclusion

This study examined how flexible vegetation influences wave-vegetation interactions and sediment suspension over rippled sandy beds. The results demonstrate that stem flexibility alters canopy-scale hydrodynamics but does not modify the dominant mechanisms governing near-bed sediment suspension when bedforms are present. Flexible vegetation canopies, which reconfigure with the oscillatory flow, limit stem-generated TKE compared with rigid vegetation. Velocity attenuation is also confined to the lower canopy, resulting in near-bed velocities and TKE levels comparable to bare-bed conditions, under the current test conditions. This is a contrast to the rigid vegetation canopies of equal canopy density and stem height and stem width, which exhibited stronger velocity attenuation over the height of the stem and in the near-bed region, whilst increasing stem-generated TKE.

The suspended sediment concentration is primarily governed by bedform processes and coherent ripple structure persists within flexible vegetation canopies across all vegetation densities and wave conditions tested. This was observed despite differences in these vegetation-induced hydrodynamics. In contrast, rigid vegetation disrupts ripple geometry through stem-scale wake interactions and scouring around individual vegetation. Vertical sediment diffusivity near the bed remains comparable across bare, flexible, and rigid vegetation cases. Vertical diffusivity appears to be controlled by ripple-induced vortex shedding. As a result, the suspended sediment concentration fits onto a single power-law relationship with U_{bed} across all vegetation types and densities considered. This unified relationship indicates that, once ripples are present, U_{bed} is the dominant control on sediment resuspension and the primary role of vegetation is to attenuate U_{bed} and therefore alter the ripple morphology. This is reinforced by the good agreement between C_0 predictions calculated following the methodology derived for bare sediment ripple beds (Green and Black, 1999; Thorne et al., 2002; Goldstein et al., 2013) using the modified shields parameter and existing formulae for ripple dimension prediction.

These findings contrast with previous studies conducted over flat beds or within denser vegetation canopies, where stem-generated TKE has been shown to enhance sediment suspension and govern near-bed resuspension behaviour. For the range of wave conditions, vegetation densities, and stem flexural rigidities investigated in this present study, results suggest that sediment resuspension in vegetated coastal environments can be described using velocity-based suspension methods, without explicit representation of vegetation-induced TKE, provided that bedforms are present. This insight offers a practical advantage for coastal management by enabling simplified, physics-based parameterisations that reduce complexity while maintaining predictive accuracy for sediment transport in coastal vegetated systems.

The present findings are most directly applicable to wave-dominated, sandy non-cohesive seabeds with vegetation properties representative of seagrasses and flexible saltmarsh species, as reflected in the *Ca* and *EI* ranges (Table 1**).** Future studies should further explore the role of different plant flexural rigidities, canopy densities, and finer-grained sediment sizes to expand the findings of this study further.

Open research

Data archiving is underway and can be made available upon request.

CRediT authorship contribution statement

K. Ions: Writing – review & editing, Writing – original draft, Validation, Methodology, Investigation, Formal analysis, Data curation. **X. Wang:** Writing – review & editing. **N. Mori:** Writing – review & editing, Funding acquisition. **D.E. Reeve:** Writing – review & editing, Supervision. **H. Karunarathna:** Writing – review & editing, Writing – original draft, Supervision, Project administration, Methodology, Funding acquisition, Conceptualization.

Declaration of competing interest

The authors declare that they have no known competing financial interests or personal relationships that could have appeared to influence the work reported in this paper.

Acknowledgements

This research is supported by the Engineering and Physical Sciences Research Council (EPSRC) UK Doctoral Training Partnership of Swansea University (EP/T517987/1) grant. We would like to thank Dr. J.M. Horrillo-Caraballo for the assistance during the experiments. KI XW and HK acknowledge Leverhulme Trust Research Grant RPG-2023-235. We also extend thanks to The Great British Sasakawa Foundation Grant No. 6365 and the Disaster Prevention Research Institute (DPRI) of Kyoto University International Collaborative Research Grant 2023IG-02 for facilitating research collaboration between Swansea University and DPRI. NM is also supported by JICA/JST SATREPS Program (JPMJSA2110). Lastly, the authors acknowledge PDRI International Collaborative Research Grant FY2023.

Appendix A

Table A1
List of experimental conditions in this study. For the cases, B1-B17 represent bare sediment bed cases, DV and SV indicate dense and sparse vegetation, and the prefix of R or F indicates rigid or flexible plant mimics.

CASE	*Hs (m)*	*T (s)*	*Ubed(m/s)*	*h/hv*	*Nv*	*φ*	*Aw (cm)*	*Aw/Sx*
B1*	0.1	1	0.11	0.66	0	0	1.79	inf
B2*	0.12	1	0.13	0.66	0	0	2.06	inf
B3*	0.15	1	0.14	0.66	0	0	2.21	inf
B4	0.1	1.5	0.18	0.66	0	0	4.25	inf
B5	0.12	1.5	0.21	0.66	0	0	4.91	inf
B6	0.15	1.5	0.23	0.66	0	0	5.43	inf
B7	0.2	1.5	0.33	0.66	0	0	7.9	inf
B8	0.1	2	0.19	0.66	0	0	5.95	inf
B9	0.15	2	0.3	0.66	0	0	9.63	inf
B10*	0.06	1	0.11	1	0	0	1.76	inf
B11*	0.08	1	0.15	1	0	0	2.34	inf
B12	0.1	1	0.18	1	0	0	2.8	inf
B13	0.06	1.5	0.15	1	0	0	3.46	inf
B14	0.08	1.5	0.21	1	0	0	4.55	inf
B15	0.1	1.5	0.25	1	0	0	5.8	inf
B16	0.06	2	0.21	1	0	0	5.45	inf
B17	0.08	2	0.28	1	0	0	6.76	inf
R-DV1*	0.1	1	0.06	0.66	342	0.67	1.48	0.25
R-DV2*	0.12	1	0.09	0.66	342	0.67	1.94	0.32
R-DV3*	0.15	1	0.11	0.66	342	0.67	2.38	0.4
R-DV4	0.1	1.5	0.14	0.66	342	0.67	3.7	0.62
R-DV5	0.12	1.5	0.17	0.66	342	0.67	4.44	0.74
R-DV6	0.15	1.5	0.22	0.66	342	0.67	5.16	0.86
R-DV7	0.2	1.5	0.25	0.66	342	0.67	5.63	0.94
R-DV8	0.1	2	0.17	0.66	342	0.67	5.73	0.96
R-DV9	0.15	2	0.26	0.66	342	0.67	8.09	1.35
R-DV10*	0.06	1	0.07	1	342	0.67	1.09	0.18
R-DV11*	0.08	1	0.09	1	342	0.67	1.71	0.29
R-DV12	0.1	1	0.12	1	342	0.67	1.53	0.26
R-DV13	0.06	1.5	0.13	1	342	0.67	2.77	0.46
R-DV14	0.08	1.5	0.15	1	342	0.67	3.62	0.6
R-DV15	0.1	1.5	0.2	1	342	0.67	4.78	0.8
R-DV16	0.06	2	0.14	1	342	0.67	5.6	0.93
R-DV17	0.08	2	0.21	1	342	0.67	6.46	1.08
R-SV1*	0.1	1	0.1	0.66	80	0.16	1.83	0.15
R-SV2*	0.12	1	0.12	0.66	80	0.16	2.08	0.17
R-SV3*	0.15	1	0.18	0.66	80	0.16	2.88	0.24
R-SV4	0.1	1.5	0.14	0.66	80	0.16	3.36	0.28
R-SV5	0.12	1.5	0.18	0.66	80	0.16	4.36	0.36
R-SV6	0.15	1.5	0.23	0.66	80	0.16	5.46	0.46
R-SV7	0.2	1.5	0.17	0.66	80	0.16	3.96	0.33
R-SV8	0.1	2	0.23	0.66	80	0.16	7.33	0.61
R-SV9	0.15	2	0.08	0.66	80	0.16	3.21	0.27
R-SV10*	0.06	1	0.1	1	80	0.16	1.91	0.16
R-SV11*	0.08	1	0.13	1	80	0.16	2.32	0.19
R-SV12	0.1	1	0.15	1	80	0.16	2.7	0.23
R-SV13	0.06	1.5	0.16	1	80	0.16	4.09	0.34
R-SV14	0.08	1.5	0.25	1	80	0.16	5.94	0.5
R-SV15	0.1	1.5	0.32	1	80	0.16	7.73	0.64
R-SV16	0.06	2	-	1	80	0.16	-	-
R-SV17	0.08	2	0.3	1	80	0.16	9.45	0.79
F-DV1	0.1	1	0.11	0.66	342	0.67	1.76	0.29
F-DV2	0.12	1	0.13	0.66	342	0.67	2.12	0.35
F-DV3	0.15	1	0.15	0.66	342	0.67	2.32	0.39

(*continued on next page*)

Table A1 (*continued*)

CASE	*Hs (m)*	*T (s)*	*Ubed(m/s)*	*h/hv*	*Nv*	*φ*	*Aw (cm)*	*Aw/Sx*
F-DV4	0.1	1.5	0.17	0.66	342	0.67	3.97	0.66
F-DV5	0.12	1.5	0.22	0.66	342	0.67	5.18	0.86
F-DV6	0.15	1.5	0.23	0.66	342	0.67	5.54	0.92
F-DV7	0.2	1.5	0.3	0.66	342	0.67	7.19	1.2
F-DV8	0.1	2	-	0.66	342	0.67	-	-
F-DV9	0.15	2	0.31	0.66	342	0.67	9.87	1.64
F-DV10	0.06	1	-	1	342	0.67	-	-
F-DV11	0.08	1	0.15	1	342	0.67	2.31	0.39
F-DV12	0.1	1	0.15	1	342	0.67	2.31	0.39
F-DV13	0.06	1.5	0.14	1	342	0.67	3.33	0.56
F-DV14	0.08	1.5	0.2	1	342	0.67	4.77	0.8
F-DV15	0.1	1.5	0.24	1	342	0.67	5.67	0.95
F-DV16	0.06	2	0.17	1	342	0.67	5.27	0.88
F-DV17	0.08	2	0.18	1	342	0.67	5.73	0.96
F-SV1	0.1	1	-	0.66	80	0.16	-	-
F-SV2	0.12	1	0.14	0.66	80	0.16	2.27	0.19
F-SV3	0.15	1	-	0.66	80	0.16	-	-
F-SV4	0.1	1.5	0.15	0.66	80	0.16	3.5	0.29
F-SV5	0.12	1.5	0.2	0.66	80	0.16	4.73	0.39
F-SV6	0.15	1.5	0.23	0.66	80	0.16	5.41	0.45
F-SV7	0.2	1.5	-	0.66	80	0.16	-	-
F-SV8	0.1	2	0.2	0.66	80	0.16	6.22	0.52
F-SV9	0.15	2	0.12	0.66	80	0.16	3.74	0.31
F-SV10	0.06	1	0.14	1	80	0.16	2.2	0.18
F-SV11	0.08	1	0.15	1	80	0.16	2.33	0.19
F-SV12	0.1	1	0.18	1	80	0.16	2.93	0.24
F-SV13	0.06	1.5	0.21	1	80	0.16	5.08	0.42
F-SV14	0.08	1.5	0.24	1	80	0.16	5.65	0.47
F-SV15	0.1	1.5	0.33	1	80	0.16	7.81	0.65
F-SV16	0.06	2	-	1	80	0.16	-	-
F-SV17	0.08	2	0.31	1	80	0.16	9.92	0.83

References

Abdelrhman, M.A., 2007. Modeling coupling between eelgrass Zostera marina and water flow. Mar. Ecol. Prog. Ser. 338, 81–96. https://doi.org/10.3354/meps338081.

Abdolahpour, M., Hambleton, M., Ghisalberti, M., 2017. The wave-driven currents in coastal canopies. J. Geophys. Res.: Oceans 122 (5). https://doi.org/10.1002/2016JC012446.

Belcher, S.E., Jerram, N., Hunt, J.C.R., 2003. Adjustment of a turbulent boundary layer to a canopy of roughness elements. J. Fluid Mech. 488, 369–398. https://doi.org/10.1017/S0022112003005019.

Boström, C., Baden, S., Bockelmann, A.C., Dromph, K., Fredriksen, S., Gustafsson, C., Rinde, E., 2014. Distribution, structure and function of Nordic eelgrass (*Zostera marina*) ecosystems: implications for coastal management and conservation. Aquat. Conserv.: Mar. Freshw. Ecosyst. 24 (3), 410–434. https://doi.org/10.1002/aqc.2424.

Bouma, T.J., de Vries, M.B., Low, E., Kusters, L., Herman, P.M.J., Tanczos, I.C., Temmerman, S., Hesselink, A., Meire, P., van Regenmortel, S., 2005. Flow hydrodynamics on a mudflat and in salt marsh vegetation: identifying general relationships for habitat characterisations. Hydrobiologia 540, 259–274.

Bradley, K., Houser, C., 2009. Relative velocity of seagrass blades: implications for wave attenuation in low-energy environments. J. Geophys. Res.: Earth Surf. 114, F01004. https://doi.org/10.1029/2007JF000951.

Clifton, H.E., 1976. Wave-Formed Sedimentary Structures—A Conceptual Model. https://doi.org/10.2110/pec.76.24.0126.

Dalrymple, R.A., Kirby, J.T., Hwang, P.A., 1984. Wave diffraction due to areas of energy dissipation. J. Waterw. Port Coast. Ocean Eng. 110 (1), 67–79. https://doi.org/10.1061/(ASCE)0733-950X.

Davies, A.G., Thorne, P.D., 2008. Advances in the study of moving sediments and evolving seabeds. Surv. Geophys. 29 (1), 1–36. https://doi.org/10.1007/s10712-008-9039-x.

De Falco, G., Ferrari, S., Cancemi, G., Baroli, M., 2000. Relationship between sediment distribution and *Posidonia oceanica* seagrass. Geo-Mar. Lett. 20 (1), 50–57. https://doi.org/10.1007/s003670000030.

den Hartog, C., 1970. The Sea-Grasses of the World. North-Holland Publishing Company, Amsterdam.

Du Toit, C.K., Sleath, J.F.A., 1981. Velocity measurements close to rippled beds in oscillatory flow. J. Fluid Mech. 112, 71–96. https://doi.org/10.1017/S002211208100030X.

Duarte, C.M., 1991. Allometric scaling of seagrass form and productivity. Mar. Ecol. Prog. Ser. 77, 289–300.

Fagherazzi, S., Bryan, K.R., Nardin, W., 2017. Buried alive or washed away: the challenging life of mangroves in the Mekong delta. Oceanography 30 (3), 48–59. https://doi.org/10.5670/oceanog.2017.313.

Feagin, R.A., Irish, J.L., Möller, I., Williams, A.M., Colón-Rivera, R.J., Mousavi, M.E., 2011. Engineering properties of wetland plants with application to wave attenuation. Coast. Eng. 58 (3), 251–255. https://doi.org/10.1016/j.coastaleng.2010.10.003.

Folkard, A.M., 2005. Hydrodynamics of model *Posidonia oceanica* patches in shallow water. Limnol. Oceanogr. 50 (5), 1592–1600. https://doi.org/10.4319/lo.2005.50.5.1592.

Fonseca, M.S., Cahalan, J.A., 1992. A preliminary evaluation of wave attenuation by four species of seagrass. Estuar. Coast. Shelf Sci. 35 (6), 565–576. https://doi.org/10.1016/S0272-7714(05)80039-3.

Fonseca, M.S., Fourqurean, J.W., Koehl, M.A.R., 2019. Effect of seagrass on current speed: importance of flexibility vs. shoot density. Front. Mar. Sci. 6, 376. https://doi.org/10.3389/fmars.2019.00376.

Furukawa, K., Wolanski, E., Mueller, H., 1997. Currents and sediment transport in mangrove forests. Estuar. Coast. Shelf Sci. 44 (3), 301–310. https://doi.org/10.1006/ecss.1996.0120.

Gambi, M.C., Nowell, A.R.M., Jumars, P.A., 1990. Flume observations on flow dynamics in *Zostera marina* (eelgrass) beds. Mar. Ecol. Prog. Ser. 61, 159–169. https://www.jstor.org/stable/24842256.

Ghisalberti, M., Nepf, H.M., 2002. Mixing layers and coherent structures in vegetated aquatic flows. J. Geophys. Res.: Oceans 107 (C2). https://doi.org/10.1029/2001JC000871.

Gijón Mancheño, A., 2016. Interaction Between Wave Hydrodynamics and Flexible Vegetation (master's thesis). TU Delft, Delft, The Netherlands.

Gintowt, N.A., Kendzierska, H., Janas, U., 2025. Seasonal dynamics of benthic infauna communities in Zostera marina meadows: effects of plant density gradients. Biology 14 (2), 153. https://doi.org/10.3390/biology14020153.

Giri, C., Ochieng, E., Tieszen, L.L., Zhu, Z., Singh, A., Loveland, T., Duke, N., 2011. Status and distribution of mangrove forests of the world using earth observation satellite data. Glob. Ecol. Biogeogr. 20 (1), 154–159. https://doi.org/10.1111/j.1466-8238.2010.00584.x.

Goldstein, E.B., Coco, G., Murray, A.B., 2013. Prediction of wave ripple characteristics using genetic programming. Cont. Shelf Res. 71, 1–15. https://doi.org/10.1016/j.csr.2013.09.020.

Grady, J.R., 1981. Properties of seagrass and sand flat sediments from the intertidal zone of St. Andrew bay, Florida. Estuaries Coasts 4, 335–344. https://doi.org/10.2307/1352158.

Green, M.O., Black, K.P., 1999. Suspended-sediment reference concentration under waves: field observations and critical analysis of two predictive models. Coast. Eng. 38 (3), 115–141. https://doi.org/10.1016/S0378-3839(99)00044-7.

Hansen, J.C.R., Reidenbach, M.A., 2012. Wave- and tidally driven flows in eelgrass beds and their effect on sediment suspension. Mar. Ecol. Prog. Ser. 448, 271–287. https://doi.org/10.3354/meps09225.

Hemminga, M.A., Duarte, C.M., 2000. *Seagrass ecology*. Cambridge University Press. Press.

Hill, J.W., Bennion, V., Lovelock, C.E., 2024. Mangrove tree strength estimated with field experiments. Ecol. Eng. 203, 107259. https://doi.org/10.1016/j.ecoleng.2024.107259.
Himes-Cornell, A., Pendleton, L., Atiyah, P., 2018. Valuing ecosystem services from blue forests: a systematic review of the valuation of salt marshes, seagrass beds and mangrove forests. Ecosyst. Serv. 30, 36–48. https://doi.org/10.1016/j.ecoser.2018.01.006.
Horppila, J., Nurminen, L., 2003. Effects of submerged macrophytes on sediment resuspension and internal phosphorus loading in lake Hiidenvesi (southern Finland). Water Res. 37 (18), 4468–4474. https://doi.org/10.1016/S0043-1354(03)00405-6.
Infantes, E., Orfila, A., Simarro, G., Terrados, J., Luhar, M., Nepf, H., 2012. Effect of a seagrass (*Posidonia oceanica*) meadow on wave propagation. Mar. Ecol. Prog. Ser. 456, 63–72. https://doi.org/10.3354/meps09754.
Ions, K., Wang, X., Reeve, D.E., Mori, N., Karunarathna, H., 2025. Submerged and emerged rigid vegetation impact on bedforms and sediment suspension under wave action. Coast. Eng. 199, 104739. https://doi.org/10.1016/j.coastaleng.2025.104739.
Koch, E.W., Gust, G., 1999. Water flow in tide- and wave-dominated beds of the seagrass *Thalassia testudinum*. Mar. Ecol. Prog. Ser. 184, 63–72. https://doi.org/10.3354/meps184063.
Keimer, K., Schürenkamp, D., Miescke, F., Kosmalla, V., Lojek, O., Goseberg, N., 2021. Ecohydraulics of surrogate salt marshes for coastal protection: Wave–vegetation interaction and related hydrodynamics on vegetated foreshores at sea dikes. J. Waterw. Port Coast. Ocean Eng. 147 (6), 04021035. https://doi.org/10.1016/j.coastaleng.2025.104739.
Koch, E.W., Barbier, E.B., Silliman, B.R., Reed, D.J., Perillo, G.M., Hacker, S.D., Wolanski, E., 2009. Non-linearity in ecosystem services: temporal and spatial variability in coastal protection. Front. Ecol. Environ. 7 (1), 29–37. https://doi.org/10.1890/080126.
Komar, P.D., Miller, M.C., 1973. The threshold of sediment movement under oscillatory water waves. J. Sediment. Res. 43 (4). https://doi.org/10.1306/74D7290A-2B21-11D7-8648000102C1865D.
Lei, J., Nepf, H., 2019. Wave damping by flexible vegetation: Connecting individual blade dynamics to the meadow scale. Coast. Eng. 147, 138–148. https://doi.org/10.1016/j.coastaleng.2019.01.008.
Lei, J., Nepf, H., 2019. Wave damping by flexible vegetation: Connecting individual blade dynamics to the meadow scale. Coast. Eng. 147, 138–148. https://doi.org/10.1016/j.coastaleng.2019.01.008.
Liu, W., Pennings, S.C., 2019. Self-thinning and size-dependent flowering of the grass *Spartina alterniflora* across space and time. Funct. Ecol. 33 (10), 1830–1841. https://doi.org/10.1111/1365-2435.13384.
Luhar, M., Nepf, H.M., 2011. Flow-induced reconfiguration of buoyant and flexible aquatic vegetation. Limnol. Oceanogr. 56. https://doi.org/10.4319/lo.2011.56.6.2003. Digital Object Identifier (D OI).
Luhar, M., Nepf, H.M., 2016. Wave-induced dynamics of flexible blades. J. Fluids Struct. 61, 20–41. https://doi.org/10.1016/j.jfluidstructs.2015.11.007.
Luhar, M., Coutu, S., Infantes, E., Fox, S., Nepf, H., 2010. Wave-induced velocities inside a model seagrass bed. J. Geophys. Res.: Oceans 115 (C12). https://doi.org/10.1029/2010JC006345.
Luhar, M., Infantes, E., Nepf, H., 2017. Seagrass blade motion under waves and its impact on wave decay. J. Geophys. Res.: Oceans 122 (5), 3736–3752. https://doi.org/10.1002/2017JC012731.
Marín-Díaz, B., Bouma, T.J., Infantes, E., 2020. Role of eelgrass on bedload transport and sediment resuspension under oscillatory flow. Limnol. Oceanogr. 65 (2), 426–436. https://doi.org/10.1002/lno.11312.
Masselink, G., Jones, R.B., 2023. Long-term accretion rates in UK saltmarshes derived from elevation difference between natural and reclaimed marshes. Mar. Geol. 467, 107202. https://doi.org/10.1016/j.margeo.2023.107202.
Masselink, G., Brown, T., Scott, T., Brodie, L., 2024. Sediment sorting within a relatively wave-exposed and sandy subtidal seagrass (*Zostera marina*) meadow. Mar. Geol. 476, 107385. https://doi.org/10.1016/j.margeo.2024.107385.
McKee, K.L., 2011. Biophysical controls on accretion and elevation change in Caribbean mangrove ecosystems. Estuar. Coast. Shelf Sci. 91 (4), 475–483. https://doi.org/10.1016/j.ecss.2010.05.001.
McKee, K.L., Cahoon, D.R., Feller, I.C., 2007. Caribbean mangroves adjust to rising sea level through biotic controls on change in soil elevation. Glob. Ecol. Biogeogr. 16 (5), 545–556. https://doi.org/10.1111/j.1466-8238.2007.00317.x.
McOwen, C.J., Weatherdon, L.V., Van Bochove, J.W., Sullivan, E., Blyth, S., Zöckler, C., Stanwell-Smith, D., Kingston, N., Martin, C.S., Spalding, M., Fletcher, S., 2017. A global map of saltmarshes. Biodivers. Data J. (5). https://doi.org/10.3897/BDJ.5.e11764.
Möller, I., Kudella, M., Rupprecht, F., Spencer, T., Paul, M., van Wesenbeeck, B.K., Wolters, G., Jensen, K., Bouma, T.J., Miranda-Lange, M., Schimmels, S., 2014. Wave attenuation over coastal salt marshes under storm surge conditions. Nat. Geosci. 7 (10), 727–731. https://doi.org/10.1038/ngeo2251.
Mori, N., Chang, C.W., Inoue, T., Akaji, Y., Hinokidani, K., Baba, S., Shimura, T., 2022. Parameterization of mangrove root structure of *Rhizophora stylosa* in coastal hydrodynamic model. Front. Built Environ. 7, 782219. https://doi.org/10.3389/fbuil.2021.782219.
Moritsch, M.M., Byrd, K.B., Davis, M., Good, A., Drexler, J.Z., Morris, J.T., Woo, I., Windham-Myers, L., Grossman, E., Nakai, G., Poppe, K.L., 2022. Can coastal habitats rise to the challenge? Resilience of estuarine habitats, carbon accumulation, and economic value to sea-level rise in a Puget Sound estuary. Estuaries Coasts 45 (8), 2293–2309. https://doi.org/10.1007/s12237-022-01087-5.
Mullarney, J.C., Henderson, S.M., 2010. Wave-forced motion of submerged single-stem vegetation. J. Geophys. Res.: Oceans 115 (C12). https://doi.org/10.1029/2010JC006448.
Mullarney, J.C., Henderson, S.M., Norris, B.K., Bryan, K.R., Fricke, A.T., Sandwell, D.R., Culling, D.P., 2017. A question of scale: how turbulence around aerial roots shapes the seabed morphology in mangrove forests of the Mekong delta. Oceanography 30 (3), 34–47. https://doi.org/10.5670/oceanog.2017.312.
Nepf, H.M., 2012. Flow and transport in regions with aquatic vegetation. Annu. Rev. Fluid Mech. 44 (1), 123–142. https://doi.org/10.1146/annurev-fluid-120710-101048.
Nielsen, P., 1986. Suspended sediment concentrations under waves. Coast. Eng. 10, 23–31. https://doi.org/10.1016/0378-3839(86)90037-2.
Nielsen, P., 1992. Coastal Bottom Boundary Layers and Sediment Transport, 4. World Scientific. https://doi.org/10.1142/9789812796035.
Paul, M., de los Santos, C.B., 2019. Variation in flexural, morphological, and biochemical leaf properties of eelgrass (*Zostera marina*) along the European Atlantic climate regions. Mar. Biol. 166, 127. https://doi.org/10.1007/s00227-019-3577-2.
Paul, M., Bischoff, C., Koop-Jakobsen, K., 2022. Biomechanical traits of salt marsh vegetation are insensitive to future climate scenarios. Sci. Rep. 12, 21272. https://doi.org/10.1038/s41598-022-25525-3.
O'Connor, M.I., Violin, C.R., Anton, A., Ladwig, L.M., Piehler, M.F., 2011. Salt marsh stabilization affects algal primary producers at the marsh edge. Wetl. Ecol. Manag. 19 (2), 131–140. https://doi.org/10.1007/s11273-010-9206-y.
Pujol, D., Serra, T., Colomer, J., Casamitjana, X., 2013. Flow structure in canopy models dominated by progressive waves. J. Hydrol. 486, 281–292. https://doi.org/10.1016/j.jhydrol.2013.01.024.
Reidenbach, M.A., Thomas, E.L., 2018. Influence of the seagrass, *Zostera marina*, on wave attenuation and bed shear stress within a shallow coastal bay. Front. Mar. Sci. 5, 397. https://doi.org/10.3389/fmars.2018.00397.
Reidenbach, M.A., Timmerman, R., 2019. Interactive effects of seagrass and the microphytobenthos on sediment suspension within shallow coastal bays. Estuaries Coasts 42, 2038–2053. https://doi.org/10.1007/s12237-019-00627-w.
Méndez-Alonzo, R., Moctezuma, C., Ordoñez, V.R., Angeles, G., Martínez, A.J., López-Portillo, J., 2015. Root biomechanics in *Rhizophora mangle*: anatomy, morphology and ecology of mangrove's flying buttresses. Ann. Bot. 115 (5), 833–840. https://doi.org/10.1093/aob/mcv002.
Ros, À., Colomer, J., Serra, T., Pujol, D., Soler, M., Casamitjana, X., 2014. Experimental observations on sediment resuspension within submerged model canopies under oscillatory flow. Cont. Shelf Res. 91, 220–231. https://doi.org/10.1016/j.csr.2014.10.004.
Rupprecht, F., Möller, I., Evans, B., Spencer, T., Jensen, K., 2015. Biophysical properties of salt marsh canopies—quantifying plant stem flexibility and above ground biomass. Coast. Eng. 100, 48–57. https://doi.org/10.1016/j.ecoleng.2016.12.030.
Rupprecht, F., Möller, I., Paul, M., Kudella, M., Spencer, T., Van Wesenbeeck, B.K., Schimmels, S., 2017. Vegetation-wave interactions in salt marshes under storm surge conditions. Ecol. Eng. 100, 301–315. https://doi.org/10.1016/j.ecoleng.2016.12.030.
Schulze, D., Jensen, K., Nolte, S., 2022. Effects of small-scale patterns of vegetation structure on suspended sediment concentration and sediment deposition in a salt marsh. Estuar. Coast. Shelf Sci. 278, 108125. https://doi.org/10.1016/j.ecss.2022.108125.
Sleath, J.F.A., 1991. Velocities and shear stresses in wave–current flows. J. Geophys. Res. 96, 15237–15244. https://doi.org/10.1029/91JC01458.
Soulsby, R.L., 1997. Dynamics of Marine Sands. Thomas Telford, London.
Soulsby, R., 1997. Dynamics of marine sands: A manual for practical applications. Thomas Telford. https://doi.org/10.1680/doms.25844.
Soulsby, R.L., Whitehouse, R.J., 2005. Prediction of Ripple Properties in Shelf Seas—Mark 2 Predictor for Time Evolution (Final Technical Report).
Swart, D.H., 1974. Offshore sediment transport and equilibrium beach profiles. Publication. Delft Hydraulics Laboratory= Publikatie-Waterloopkundig Laboratorium.
Tang, C., Lei, J., Nepf, H.M., 2019. Impact of vegetation-generated turbulence on the critical, near-bed, wave-velocity for sediment resuspension. Water Resour. Res. 55 (7), 5904–5917. https://doi.org/10.1029/2018WR024335.
Temmerman, S., Meire, P., Bouma, T.J., Herman, P.M., Ysebaert, T., de Vriend, H.J., 2013. Ecosystem-based coastal defence in the face of global change. Nature 504 (7478), 79–83. https://doi.org/10.1038/nature12859.
Thielicke, W., Sonntag, R., 2021. Particle image velocimetry for MATLAB: accuracy and enhanced algorithms in PIVlab. J. Open Res. Softw. https://doi.org/10.5334/jors.334.
Thorne, P.D., Davies, A.G., Bell, P.S., 2009. Observations and analysis of sediment diffusivity profiles over sandy rippled beds under waves. J. Geophys. Res.: Oceans 114 (C2). https://doi.org/10.1029/2008JC004944.
Thorne, P.D., Williams, J.J., Davies, A.G., 2002. Suspended sediments under waves measured in a large-scale flume facility. J. Geophys. Res.: Oceans 107 (C8). https://doi.org/10.1029/2001JC000988.
Tinoco, R.O., Coco, G., 2014. Observations of the effect of emergent vegetation on sediment resuspension under unidirectional currents and waves. Earth Surf. Dyn. 2 (1), 83–96. https://doi.org/10.5194/esurf-2-83-2014.
Tinoco, R.O., Coco, G., 2016. Observations of the effect of emergent vegetation on sediment resuspension under unidirectional currents and waves. Earth Surf. Dyn. 2 (1), 83–96. https://doi.org/10.5194/esurf-2-83-2014.
Tinoco, R.O., Coco, G., 2018. Turbulence as the main driver of resuspension in oscillatory flow through vegetation. J. Geophys. Res.: Earth Surf. 123 (5), 891–904. https://doi.org/10.1002/2017JF004504.

Tseng, C.Y., Tinoco, R.O., 2021. A two-layer turbulence-based model to predict suspended sediment concentration in flows with aquatic vegetation. Geophys. Res. Lett. 48 (3), e2020GL091255. https://doi.org/10.1029/2021WR030776.

van Rijn, L.C., 1984. Sediment transport, part 1: bed load transport. J. Hydraul. Eng. 110 (10), 1431–1456. https://doi.org/10.1061/(ASCE)0733-9429(1984)110:10(1431).

van Rijn, L.C., 2007a. Unified view of sediment transport by currents and waves. II: suspended transport. J. Hydraul. Eng. 133 (6), 668–689. https://doi.org/10.1061/(ASCE)0733-9429(2007)133:6(668).

van Rijn, L.C., 2007b. Unified view of sediment transport by currents and waves. III: graded beds. J. Hydraul. Eng. 133 (7), 761–775. https://doi.org/10.1061/(ASCE)0733-9429(2007)133:7(761).

van Veelen, T.J., Fairchild, T.P., Reeve, D.E., Karunarathna, H., 2020. Experimental study on vegetation flexibility as control parameter for wave damping and velocity structure. Coast. Eng. 157, 103648. https://doi.org/10.1016/j.coastaleng.2020.103648.

van Veelen, T.J., Karunarathna, H., Reeve, D.E., 2021. Modelling wave attenuation by quasi-flexible vegetation. Coast. Eng. 164, 103820. https://doi.org/10.1016/j.coastaleng.2020.103820.

van Veelen, T.J., Nepf, H., Hulscher, S.J., Borsje, B.W., 2025. The thresholds of sediment resuspension within emergent vegetation under combined wave–current conditions—a flume experiment. Coast. Eng., 104727 https://doi.org/10.1016/j.coastaleng.2025.104727.

Weitzman, J.S., Zeller, R.B., Thomas, F.I.M., Koseff, J.R., 2015. The attenuation of current- and wave-driven flow within submerged multi-specific vegetative canopies. Limnol. Oceanogr. 60, 1855–1874. https://doi.org/10.1002/lno.10121.

Widdows, J., Pope, N.D., Brinsley, M.D., Asmus, H., Asmus, R.M., 2008. Effects of seagrass beds (Zostera noltii and Z. marina) on near-bed hydrodynamics and sediment resuspension. Mar. Ecol. Prog. Ser. 358, 125–136. https://doi.org/10.3354/meps07338.

Williams, P.B., Kemp, P.H., 1971. Initiation of ripples on flat sediment beds. J. Hydraul. Div. 97 (4), 505–522. https://doi.org/10.1061/JYCEAJ.0002932.

Yang, J.Q., Chung, H., Nepf, H.M., 2016. The onset of sediment transport in vegetated channels predicted by turbulent kinetic energy. Geophys. Res. Lett. 43 (21), 11261–11269. https://doi.org/10.1002/2016GL071092.

Worthington, T.A., Andradi-Brown, D.A., Bhargava, R., Buelow, C., Bunting, P., Duncan, C., Spalding, M., 2020. Harnessing big data to support the conservation and rehabilitation of mangrove forests globally. One Earth 2 (5), 429–443. https://doi.org/10.1016/j.oneear.2020.04.018.

Xu, Y., Nepf, H., 2020. Measured and predicted turbulent kinetic energy in flow through emergent vegetation with real plant morphology. Water Resour. Res. 56 (12), e2020WR027892. https://doi.org/10.1029/2020WR027892.

Yang, S.L., 1998. The role of Scirpus marsh in attenuation of hydrodynamics and retention of fine sediment in the Yangtze estuary. Estuar. Coast. Shelf Sci. 47 (2), 227–233. https://doi.org/10.1006/ecss.1998.0348.

Zhang, Y., Nepf, H., 2019. Wave-driven sediment resuspension within a model eelgrass meadow. J. Geophys. Res.: Earth Surf. 124 (4), 1035–1053. https://doi.org/10.1029/2018JF004984.

Zhang, Y., Tang, C., Nepf, H., 2018. Turbulent kinetic energy in submerged model meadows under oscillatory flow. Water Resour. Res. 54 (3), 1734–1750. https://doi.org/10.1002/2017WR021732.

Zhu, M., Zhu, M., Zhu, G., Nurminen, L., Wu, T., Deng, J., Zhang, Y., Ventelä, A.M., 2015. The influence of macrophytes on sediment resuspension and the effect of associated nutrients in a shallow and large lake (lake Taihu, China). PLoS One 10 (6), e0127915. https://doi.org/10.1371/journal.pone.0127915.

Lowe, R.J., Koseff, J.R., Monismith, S.G., 2005. Oscillatory flow through submerged canopies: 1. Velocity structure. J. Geophys. Res. Oceans. 110 (C10). https://doi.org/10.1029/2004JC002788.

Sleath, J.F., 1995. Sediment transport by waves and currents. J. Geophys. Res. Oceans. 100 (C6), 10977–10986. https://doi.org/10.1029/95JC00140.